IRAQI JOURNAL OF APPLIED PHYSICS

The *Iraqi Journal of Applied Physics (IJAP)* is a peer reviewed journal of high quality devoted to the publication of original research papers from applied physics and their broad range of applications. IJAP publishes quality original research papers, comprehensive review articles, survey articles, book reviews, dissertation abstracts in physics and its applications in the broadest sense. It is intended that the journal may act as an interdisciplinary forum for Physics and its applications. Innovative applications and material that brings together diverse areas of Physics are particularly welcome. Review articles in selected areas are published from time to time. It aims to disseminate knowledge; provide a learned reference in the field; and establish channels of communication between academic and research experts, policy makers and executives in industry, commerce and investment institutions. IJAP is a quarterly specialized periodical dedicated to publishing original papers, letters and reviews in: Applied & Nonlinear Optics, Applied Mechanics & Thermodynamics, Digital & Optical Communications, Electronic Materials & Devices, Laser Physics & Applications, Plasma Physics & Applications, Quantum Physics & Spectroscopy, Semiconductors & Optoelectronics, and Solid State Physics & Applications

SPONSORED AND PUBLISHED BY
THE IRAQI SOCIETY FOR ALTERNATIVE AND RENEWABLE ENERGY SOURCES & TECHNIQUES (I.S.A.R.E.S.T.)

IRAQI JOURNAL OF APPLIED PHYSICS
" INSTRUCTIONS TO AUTHORS "

CONTRIBUTIONS

Contributions to be published in this journal should be original research works, i.e., those not already published or submitted for publication elsewhere, individual papers or letters to editor.

SUBMISSION OF MANUSCRIPTS

Manuscripts should be submitted to the editor at the mailing address:

Iraqi Journal of Applied Physics
Editorial Board
P. O. Box 55259, Baghdad 12001, IRAQ, submission@ijap.org , editor@ijap.org

MANUSCRIPTS

Two hard copies with soft copy on a compact disc (CD) should be submitted to Editor in the following configuration:

- Double-spaced one-side A4 size with 2.5 cm margins of all sides
- Times New Roman font (16pt bold for title, 14pt bold for names, 12pt bold for headings, 12pt regular for text)
- Letters should not exceed 10 pages, papers should not exceed 20 pages and reviews are up to author.
- Manuscripts presented in English only are accepted.
- English abstract not exceed 150 words
- 4 keywords (at least) should be maintained on (PACS preferred)
- Author(s) should express all quantities in SI units
- Equations should be written in equation form (*italic* and symbolic)
- Figures and Tables should be separated from text
- Figures and diagrams can be submitted in colors for assessment and they will be returned to authors after provide printable copies
- Charts should be indicated by the software used for
- Only original or high-resolution scanner photos are accepted
- For electronic submission, articles should be formatted with MS-Word software.

AUTHOR NAMES AND AFFILIATIONS

It is IJAP policy that all those who have participated significantly in the technical aspects of a paper be recognized as co-authors or cited in the acknowledgments. In the case of a paper with more than one author, correspondence concerning the paper will be sent to the first author unless staff is advised otherwise.

Author name should consist of first name, middle initial, last name. The author affiliation should consist of the following, as applicable, in the order noted:

- Company or college (with department name or company division)
- Postal address
- City, state, zip code
- Country name
- Telephone, and e-mail

REFERENCES

The references should be brought at the end of the article, and numbered in the order of their appearance in the paper. The reference list should be cited in accordance with the following examples:

[1] X. Ning and M.R. Lovell, "On the Sliding Friction Characteristics of Unidirectional Continuous FRP Composites", *ASME J. Tribol.*, 124(1) (2002) 5-13.
[2] M. Barnes, "Stresses in Solenoids", *J. Appl. Phys.*, 48(5) (2001) 2000–2008.
[3] J. Jones, "Contact Mechanics", Cambridge University Press (Cambridge, UK) (2000), Ch.6, p.56.
[4] Y. Lee, S.A. Korpela and R. Horne, "Structure of Multi-Cellular Natural Convection in a Tall Vertical Annulus", Proc. 7th International Heat Transfer Conference, U. Grigul et al., eds., Hemisphere (Washington DC), 2 (1982) 221–226.
[5] M. Hashish, "Waterjet Technology Development", High Pressure Technology, PVP-Vol. 406 (2000), 135-140.
[6] D.W. Watson, "Thermodynamic Analysis", ASME Paper No. 97-GT-288 (1997).
[7] C.Y. Tung, "Evaporative Heat Transfer in the Contact Line of a Mixture", Ph.D. thesis, Rensselaer Polytechnic Institute, Troy, NY (1982).

PROOFS

Authors will receive proofs of papers and are requested to return one corrected hard copy with a WORD copy on a compact disc (CD). New materials inserted in the original text without Editor permission may cause rejection of paper.

COPYRIGHT FORM

Author(s) will be asked to transfer copyrights of the article to the Journal soon after acceptance of it. This will ensure the widest possible dissemination of information.

OFFPRINTS

Authors will receive offprints free of charge and any additional offprints can be ordered.

SUBSCRIPTION AND ORDERS

Annual fees (4 issues per year) of subscription are:

- 50 US$ for individuals inside Iraq.
- 100 US$ for establishments inside Iraq.
- 100 US$ for individuals abroad.
- 200 US$ for establishments abroad.

Fees are reduced by 25% for I.S.A.R.E.S.T. members. Orders of issues can be submitted by contacting the editor-in-chief or editorial office at **subscription@ijap.org** to maintain the address of issue delivery and payment way.

Numerical Model to Estimate the Potential Changes within Laser-Solid Surface Interaction Zone

Noor I. Naji
Abdul-Mutalib I. Ahmed

School of Applied Sciences,
University of Technology,
Baghdad, Iraq

In this work, a model is proposed to provide an estimation of the temporal and spatial changes of the potential within the interaction zone between laser and metal surface. The model depends on the real experimental data which were measured around the interaction zone. This model provides an estimation of the charge involved and considers the presence of the hole created by the interaction. For the first time, it provides the spatial and the temporal variation of the potential which reflects the electric forces and temperature at the interaction zone. It also gives a clear insight of the position of the Knudsen layer. The estimated maximum potential is more than ten times the potential at the surface boundary. This implies that surface potential is due to the interaction of the surface with the plasma rather than the usually believed thermionic emission.

Keywords: Laser-solid interaction, Poisson's equation, Knudsen layer, Plasma dynamics
Received: 16 April 2010, **Revised**: 28 May 2010, **Accepted**: 4 June 2010

1. Introduction

When intense laser radiation impinges on a solid target with initial density ρ_s, hot plasma is formed at the surface. Above certain threshold intensity, depending on the wavelength of the laser and material properties, breakdown occurs, i.e., free electrons are created in the irradiated material [1]. Up to date, the procedure, by which the very first free electron is produced, is not recognized precisely. The photon energy of the laser light is not nearly high enough to ionize the atoms or molecules, so direct photoionization cannot occur. As well, the photon energy of laser light is not high enough for multi-photon ionization. Other ionization mechanisms have been proposed, such as stimulated Raman scattering (SRS) [2]. It is most likely, that due to background radiation or impurity effects, free electrons are already present. Whatever the origin of the initial electron, it collides with another atom and ionizes it, creating yet another free electron. One electron becomes multiple electrons, each gaining energy from the radiation field and then ionizing other atoms. The concentration of free electrons increases rapidly and at high enough light intensities, results is the formation of a strongly absorbing layer at the surface of the target.

In order to produce any effect on the material by the laser radiation, laser light must be absorbed. A laser-induced process is thermally activated if the thermalization of the extinction excitation energy is fast compared to the initial processing step (i.e., pulse duration) [3-8]. In such a case, laser treatment is thermal and the laser is simply considered as a heat source. In metals, light is absorbed within 10^{-10}-10^{-14}s [9].

As the laser energy is absorbed, it is transformed into thermal energy by the plasma electrons which carry the energy deeper into the target by electron heat diffusion. At the same time, expansion of the heated material sets in and leads to the formation of an ablative electron heat wave. In a high-Z material, competition between electron heat conduction and conversion into primary x-rays modifies this heat wave. The conversion layer, typically has a high temperature (~1keV) and a low density (~0.1g/cm^3) and is thereby optically thin to the radiation generated there [10].

Focusing a strong laser beam into plasma can considerably influence the plasma's electron temperature and density. This renders the measured values of these parameters useless. The electric field of the intense laser beam can heat electrons in the plasma. This takes place via the process of inverse Bremsstrahlung, which will be introduced later. Kunze [11] estimated the relative change in electron temperature due to heating by the laser beam. The laser pulse length

 ISSN 1813-2065 Printed in IRAQ

is assumed to be long enough to heat the electrons, but too short for the electrons to transfer this heat to the heavy particles. This estimation assumes the laser beam not to affect the absorption coefficient of plasma. This is true if the maximum kinetic energy that a free electron can gain in the radiation field is less than the photon energy [12].

2. Modeling

The Poisson's equation for potential inside the plasma can be written as:

$$\nabla^2 V = -\frac{\rho}{\varepsilon_\circ} \qquad (1)$$

where ∇^2 is the Laplacian operator, V is the potential and ρ is space charge density.

There are many elegant analytical solutions to Poisson's equation in special geometries, but nowadays, real problems are usually solved numerically. Computers and software are now so powerful that it can be easier to obtain a computer solution than to find the exact one in reference books. The finite-difference method (FDM) was used to give the governing partial differential equation for a particular electromagnetic problem. The first step involved in the application of the FDM is [13] dividing the domain of interest into a grid (usually rectangular) in one, two or three dimensions; $V(x,y,z)$, which is a three dimensional (3D) solution, $V(x,y)$, which is a two dimensional (2D) solution (no z-variation), and $V(x)$, which is a one dimensional (1D) solution (no y or z-variation). The second step is developing algebraic equations, which approximate the partial derivatives in the governing equations (difference equations). The final step is solving the set of algebraic equations.

To solve the Poisson's equation numerically, the region of interest can be divided into rectangular grid over which the difference equation approximations to the 2nd order derivatives are defined. The grid points located on the boundaries represent fixed nodes where the potential is known [13,14]. The internal grid points from the boundary are defined as free nodes where the potential must be computed. The grid points are labeled in the x-direction as i, i+1, i+2, etc, and in the y-direction j, j+1, j+2, etc. In other words, we will write the equations at all internal nodes of a grid with a regular step size, h, in the x-direction as Δx, and in the y-direction, as Δy as shown in Fig. (1).

In order to solve Poisson's equation, finite differences method (FDM) is used, and the approximations to model the governing equation are based on forward-difference in time and central-difference in space. The 2D Poisson's equation in rectangular coordinates is [15]:

$$\nabla^2 V = \frac{\partial^2 V}{\partial x^2} + \frac{\partial^2 V}{\partial y^2} = -\frac{\rho}{\varepsilon_\circ} \qquad (2)$$

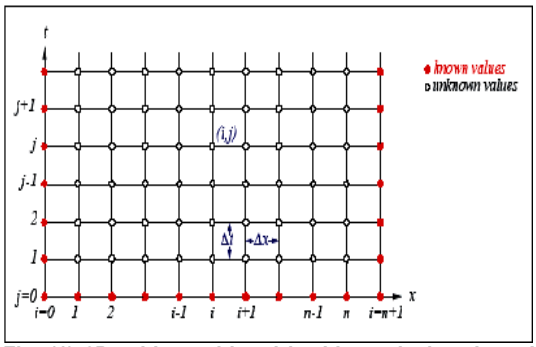

Fig. (1) 2D grid considered in this analysis, where *i* is spatial index and *j* temporal index [13]

Considering a rectangular region defined by $0 \le x \le a$ and $0 \le y \le b$ enclosed by conductors of known potential $V(x,y)$ and known charge distribution throughout $\rho(x,y)$, the required derivatives in the 2D Poisson's equation are:

$$\frac{\partial^2 V}{\partial x^2} = \frac{\partial}{\partial x}\left(\frac{\partial V}{\partial x}\right) \text{ and } \frac{\partial^2 V}{\partial y^2} = \frac{\partial}{\partial y}\left(\frac{\partial V}{\partial y}\right) \qquad (3)$$

The 1st order partial derivatives with respect to x and y can first be defined on either side of the grid point (i,j) as:

$$\left.\frac{\partial V}{\partial x}\right|_{i-\frac{1}{2},j} \approx \frac{V_{i,j} - V_{i-1,j}}{\Delta x} \qquad \left.\frac{\partial V}{\partial y}\right|_{i,j-\frac{1}{2}} \approx \frac{V_{i,j} - V_{i,j-1}}{\Delta y}$$

$$\left.\frac{\partial V}{\partial x}\right|_{i+\frac{1}{2},j} \approx \frac{V_{i+1,j} - V_{i,j}}{\Delta x} \qquad \left.\frac{\partial V}{\partial y}\right|_{i,j+\frac{1}{2}} \approx \frac{V_{i,j+1} - V_{i,j}}{\Delta y}$$

The approximations of the 1st order derivatives on either side of grid point (i,j) can then be used to approximate the 2nd order partial derivatives with respect to x and y as:

$$\left.\frac{\partial^2 V}{\partial x^2}\right|_{i,j} \approx \frac{\left.\frac{\partial V}{\partial x}\right|_{i+\frac{1}{2},j} - \left.\frac{\partial V}{\partial x}\right|_{i-\frac{1}{2},j}}{\Delta x} \qquad (4a)$$

$$\left.\frac{\partial^2 V}{\partial y^2}\right|_{i,j} \approx \frac{\left.\frac{\partial V}{\partial y}\right|_{i,j+\frac{1}{2}} - \left.\frac{\partial V}{\partial y}\right|_{i,j-\frac{1}{2}}}{\Delta y} \qquad (4b)$$

Inserting the 1st order derivative approximations and collecting terms yields the 2nd order derivative approximations, yield

$$\left.\frac{\partial^2 V}{\partial x^2}\right|_{i,j} \approx \frac{1}{\Delta x^2}[V_{i+1,j} - 2V_{i,j} + V_{i-1,j}] \qquad (5a)$$

$$\left.\frac{\partial^2 V}{\partial y^2}\right|_{i,j} \approx \frac{1}{\Delta y^2}[V_{i+1,j} - 2V_{i,j} + V_{i-1,j}] \qquad (5b)$$

Inserting the 2nd order derivative approximations in Poisson's equation gives:

$$\frac{V_{i+1,j} - 2V_{i,j} + V_{i-1,j}}{\Delta x^2} + \frac{V_{i,j+1} - 2V_{i,j} + V_{i,j-1}}{\Delta y^2} = -\frac{\rho}{\varepsilon_\circ} = B \qquad (6)$$

Given a square grid ($\Delta x = \Delta y = h$), the equation above is reduced to:

$$V_{i+1,j} + V_{i-1,j} + V_{i,j-1} - 4V_{i,j} = -\frac{h^2 \rho_{i,j}}{\varepsilon_\circ} \quad (7)$$

which is a square-grid 2D Poisson's equation

3. Experimental and Model Assumptions

Previous experimental results [16-21] were used for feeding the mathematical model with the required data to solve the equations involved. A solid stainless-steel 304 sample was irradiated by Nd:YAG laser pulses with intensity of I=12.4MW/cm^2 and wavelength λ=1.069μm. The laser was focused on spot of area A=1.38x10^{-3}cm^2 using a 10cm focusing lens [17]. A surface voltage is generated during the interaction between laser pulse and the sample [20]. A floating potential probe was used at a distance 3mm away from the sample surface to measure the potential of the plasma generated [18].

To start the analytical modeling of the experimental results, as well as to provide a solution of the problem, several assumptions are made. The material is considered as a layer that first melts then evaporates, where the skin depth represents thickness of this layer and the spot area represents the area of this layer. The system is placed into an evacuated chamber where the right and left boundary voltages (V_{bR} and V_{bL}) are zero by neglecting the charge loss produced from attraction of charge with surface. Therefore, the net charge, not the positive or the negative charge, is considered because the data taken from reference [52] represent the net charge. As well, the ionization by absorption is neglected. Also, no time delay between the charge at the boundary and the interaction zone occurs. This is needed for proper time analysis. As well, the charge is not accumulated at the interaction zone. This is true only for high vacuum. We assume that the problem is spatially 3D (x,y,z) and because of symmetry around z we have considered (x,z) for simplicity and reducing matrix size and time of calculation. We have used Cartesian coordinates because the charge distribution and motion is not a point source or cylindrical.

4. Model Parameters

The considered model needs many predefined parameters as well as numerical solutions of Poisson's equation.

4.1 Boundary Conditions Consideration

The values of the boundary conditions are taken as:

(a) Metal surface potential boundary data values are provided by reference [20]. This potential is generated from the reaction of the St-St. 304 sample with the Nd:YAG laser pulses of incident intensity 12.4 MW/cm^2. Using least square fitting (LSF) to represent these results with polynomials yields:

$V_1(t)$ = 8.758231326297914e+023t^6 - 9.647570877481166e+020t^5 + 4.3214683770712e+017t^4 + 1.004569463264522e+014t^3 + 1.274971036417507e+010t^2 - 8.371153279949487e+005t + 2.221652415436611e+001 *for* $0 \le t \le t_1$

$V_2(t)$ = -4.216190398182638e+010t^3 + 4.106638304623091e+007t^2 - 1.283412744333760e+004t + 1.211358590639905e+000 *for* $t_1 \le t \le t_2$

$V_3(t)$ = 1.058336673315529e+00t^2 - 8.700171524786168e+001t - 3.133347479914106e-002 *for* $t_2 \le t \le t_3$

where t_1, t_2 and t_3 are selected times on the potential-time curve

---

(b) The boundary data at a distance of 3mm away from the surface is taken from the experimental result of reference [18], which measured the temporal voltage using three floating probes: one single cylindrical and two circular (4.5mm and 9mm in diameter). These results are collected and interpolated as temporal and spatial voltages and they represent the potential over a lateral distance of 9mm.

The dimensions of the target are 5×2mm^2, therefore, we have selected the potentials over a central distance of 5mm instead of 9mm and for the same durations. They are considered as the upper boundary conditions.

4.2 The Charge Consideration

We get the values of the charge density from two resources; the first is the values of charge density for different time and space from the center point where the laser interaction with solid. We have integrated the data as:

$$\rho(t) = \int_{x=-4.9}^{4.9} \rho(x,t)dx \quad (8)$$

This charge is assumed to exist in the hole based on the following assumption from charge reservation law:

$$Q_{probe} = Q_{hole}$$
$$\rho_{probe} A_{probe} = \rho_{hole} A_{hole} \quad (9)$$

ISSN 1813-2065 Printed in IRAQ

where ρ_{probe}, ρ_{hole} and A_{probe}, A_{hole} are charge densities and surface areas of probe and hole, respectively

This charge may be distributed on the first layer of the hole, or overall the layers of the hole.

For the first layer

$$\left(\frac{\int \rho_{probe}}{H_{w1st}}\right)(L_{probe}t_{probe}) = \rho_{hole}(hkH_w) \quad (10a)$$

where H_{w1st} and H_w are the number of points of 1st layer (hole) and one layer, respectively, L and t are the length and thickness of the probe, respectively

For all layers

$$\left(\frac{\int \rho_{probe}}{H_{wall}}\right)(L_{probe}t_{probe}) = \rho_{hole}(hkH_w) \quad (10b)$$

The second resource is using thermal emission as we have calculated the total current density as:

$$J = A^* T^2 exp\ (-E_\omega / k_b T) \quad (11)$$

where A^* is Richardson constant, T is the temperature, E_ω is the work function. The electronic current density can be obtained by:

$J_e = A^* T^2\ exp\ (-E_\omega / k_b T) = 138.936$ A/cm^2

$I = J$ x $A = 736.365036397\text{x}10^{-3}$ A

$Q = I$ x $t_{layer} = 3788.64252135\text{x}10^{-9}$ C

The charge appears to be very small compared to that calculated from probe measurements. Therefore, we use the charge from these probe measurements.

4.3 Hole Size Consideration

Both fixed hole size of (1x1) mm and variable hole size can be considered. It was taken from previous heat model of reference [21] who considered removing a skin layer according to the deposited variable heat delivered by the laser source. The number of layers is temporally varied and changes as:

$$\frac{\Delta n}{\Delta t} = -9.6938e+024t^6 + 2.6055e+023t^5 - 6.3024e+020t^4 + 6.1694e+017t^3 - 2.9029e+014t^2 + 5.6906e+010t + 30932$$

We have derived the size from the following equation:

Z_H (size of hole) = n_L (number of layers at that time) x Z_L (size of layer)

where Z_L (size of layer) = δ (skin depth) x A (spot area)

The skin depth = 10^{-7}cm, and the spot area = $1.38\text{x}10^{-3}$cm^2.

This is satisfactory if we are looking for the variation of voltage over all space over the surface up to upper boundary.

5. Results and Discussion

The potential over the surface up to the boundary is derived by solving Poisson's equation numerically

$$\nabla^2 V = -\frac{\rho}{\varepsilon_\circ} \quad (12)$$

The 2D Poisson's equation in rectangular coordinates is

$$\nabla^2 V = \frac{\partial^2 V}{\partial x^2} + \frac{\partial^2 V}{\partial y^2} = -\frac{\rho}{\varepsilon_\circ} \quad (13)$$

according to the numerical analysis given in advance. A nodal grid is created and used in the derivation of the finite difference equations. A grid is spaced every $5\text{x}10^{-3}$/d cm along the horizontal and vertical axis to ensure that at least 31 nodes are used in obtaining the potential distribution as shown in Fig. (2).

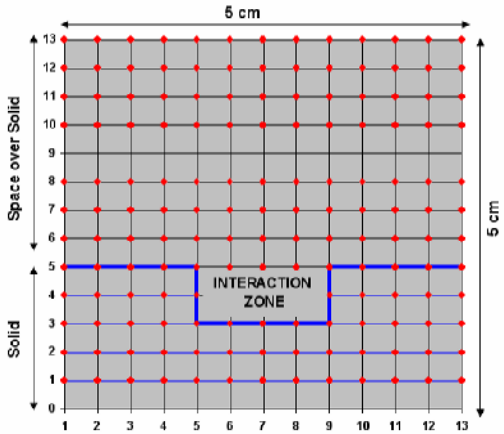

Fig. (2) Nodal grid formed in order to derive the finite difference equations

We have used 31×31 grid size to represent reasonably the actual size 5×5mm and 2mm of the metal surface. Execution of a program with this size of grid is fast since matrix size is not large. Although the program is made flexible to any size, but MATLAB for larger size would be slow.

The charges collected on the probes are considered to be the same as in the hole. This is calculated as:

$$Q_{(t)} = \rho_{probe\,(t)} L = \rho_{hole\,(t)} W \quad (14)$$

where L is the boundary length, W is the hole length, $\rho_{probe(t)}$ is the temporal charge density on the probe and $\rho_{hole(t)}$ is the temporal charge density in the hole

This charge may be divided equally on the first layer of the hole points or may be divided entirely over all the hole size (2D).

Analysis of the plasma potential production from interaction of a laser beam with a workpiece is based on development of a two-dimensional model for the geometry shown in Fig. (3). The laser beam is characterized by its wavelength λ, the beam spot radius ω_0 at the

surface, the skin depth δ, and the power density I within the spot. The workpieces were secured by a rectangular plate with a square hole in the middle, so that the laser beam could irradiate the exposed workpiece in the middle of the clamp plate.

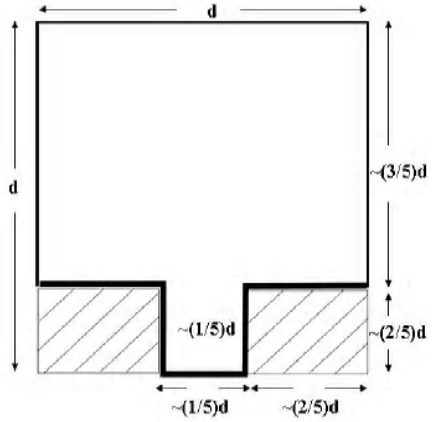

Fig. (3) Description of the boundary conditions of the mathematical model used in this work

The model described in this work explains a physical matter that can be described as a material (St. St. 304) of 2mm thickness and 5mm length, three probes (single cylindrical, and two ring probes of 9mm and 4.5mm diameters) at a distance of 3mm from the target, where the values produced from these probes were assumed as boundary conditions for the upper limits of the model and the boundary condition of the lower limit of the model was taken from reference [17]. Finally, the boundary conditions on the left and right side of the mathematical model has been assumed zero considering that the system is located in an evacuated chamber. The results have taken into account all the variables mentioned above according to the block diagram shown in Fig. (4).

The problem is solved with charge density Poisson's equation. We have solved the problem when the charge density is in the first layer and we consider a fixed hole size (1×1mm) and with only metal surface potential boundary data values as shown in Fig. (5).We have also solved the problem in the same case as before but with metal surface potential boundary data values and with boundary data at 3mm away from the surface as shown in Fig. (6).

The problem is solved when the charge density is in all layer and we consider a fixed hole size (1×1mm) and with only metal surface potential boundary data values as shown in Fig. (7).We have also solved the problem in the same case as before but with metal surface potential boundary data values and with boundary data at 3mm away from the surface as shown in Fig. (8).

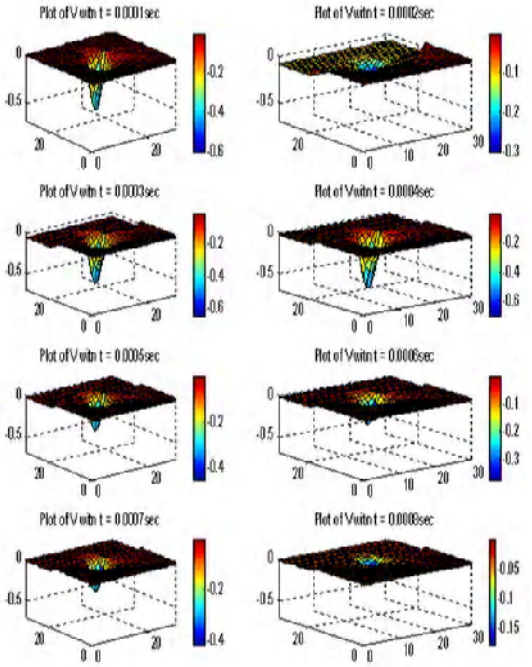

Fig. (5) The solution of the problem when the charge density is in the first Layer and considering a fixed hole size (1×1mm) and with only metal surface potential boundary data values

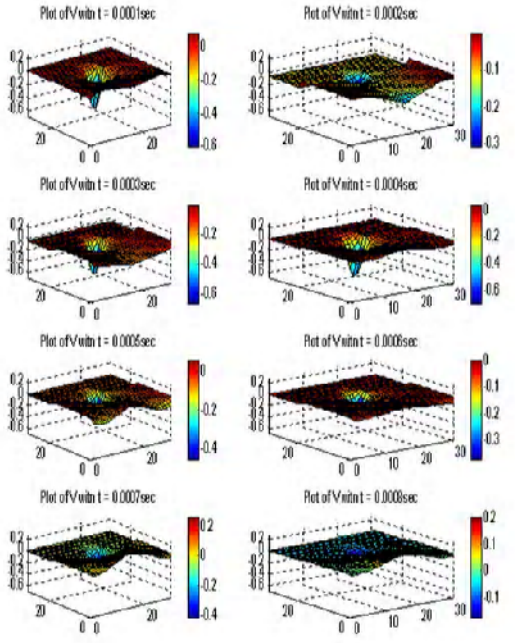

Fig. (6) The solution of the problem in the same case as before but with metal surface potential boundary data values and with boundary data a 3mm away from the surface

We also have solved the problem with hole, and we may consider a variable hole size with time but with only metal surface potential boundary data values as shown in Fig. (9). We have solved the problem in the same case as before but with metal surface potential boundary data values and with boundary data at 3mm away from the surface as shown in Fig. (10).

The case in Fig. (5) represents the potential in vacuum with no upper boundary condition. Also it represents a true experimental case at the early stage of the pulse where the mass removal is small (no proper hole).The variation of the potential with time shows clearly the stages of plum dynamic. The maximum voltage peak is about ten times the voltage of the surface boundary at t=0.001sec. At all other times the surface potential does not affect the plasma potential but only in the part near the surface.

The upper boundary in Fig. (6) does not influence the result of Fig. (5). This reflects that the potential peak near the surface is not smoothed by the upper boundary. The effect of the boundary is to change the potential distribution near the boundary since the charge is distributed in the boundary over a very large distance compared to the interaction zone.

The hole creation usually represents the extraction process that starts rapidly at the beginning of the pulse, then decays with pulse decay. Although we have assumed a constant size (1×1mm) which represents the ultimate size. The presence of hole seems to influence the potential distribution since the changes will be distributed over a greater area. The maximum peak is about 30 times the peak of the surface boundary. The effect of upper boundary in Fig. (8) only influences the region close to the boundary. This is same as in Fig. (6).

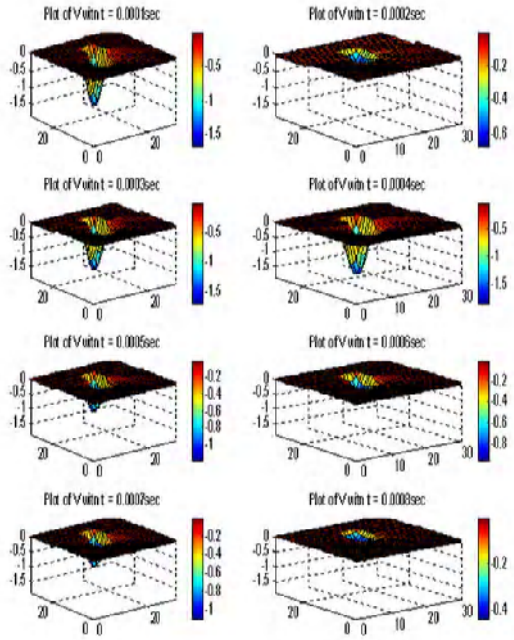

Fig. (7) The solution of the problem when the charge density is in all Layers and considering a fixed hole size (1×1mm) and with only metal surface potential boundary data values

The case of Fig. (9) represents the actual simulation of the interaction process, where the created hole size depends on the laser intensity. The potential appears to stay almost constant but the width varies with size of the hole. The width of the potential always increases with hole size.

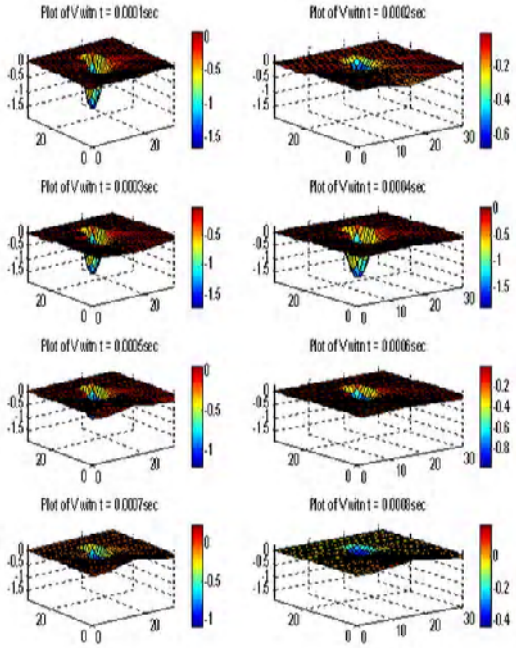

Fig. (8) The solution of the problem in the same case as before but with Metal surface potential boundary data values and with boundary data at 3mm away from the surface

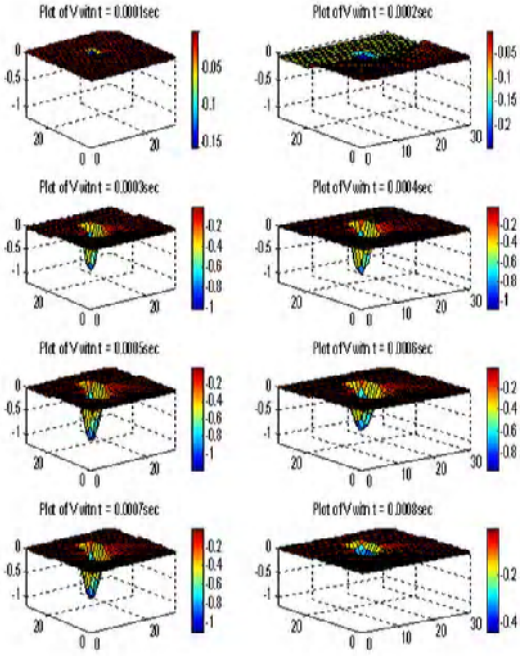

Fig. (9) The solution of the problem with hole, and we may consider a variable hole size with time but with only metal surface potential boundary data values

The effect of applying upper boundary with dynamic hole creation is presented in Fig. (10).

This boundary still only influence the region close the boundary, as in Fig. (6) and Fig. (8).

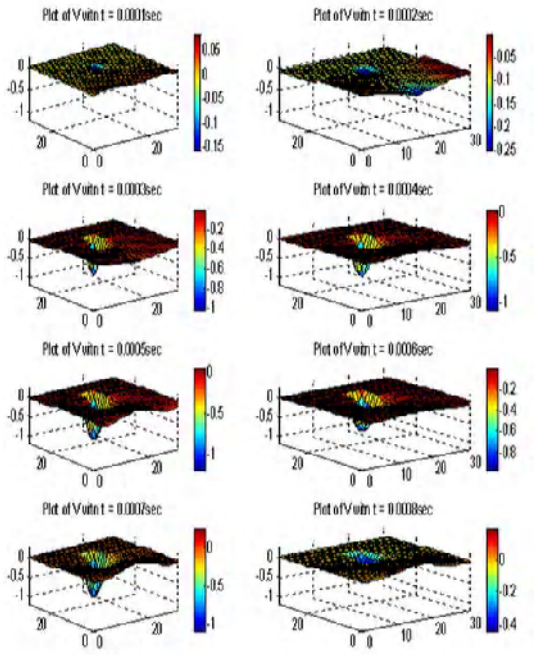

Fig. (10) The solution of the problem in the same case as before but with metal surface potential boundary data values and with boundary data at 3mm away from the surface

6. Conclusions

According to the results obtained from this work, we can conclude that a large change in the potential values appears within the interaction zone. This will cause a large electric field. This means that there is a large force acts on the charges leading to a large acceleration and collision and therefore provides good ionization and absorption conditions. As well, the most important advantage of this method is to clearly define the position of the Knudsen layer, which defines the region where the density, velocity and pressure change dramatically. We believe that this layer could be studied further using this potential method. For comparison, we have calculated the potential where boundary voltage, charge and hole are removed. The estimated maximum potential peak is ten times the surface potential. This definitely concludes that the surface potential is not a thermoionic emission type. This is also supported by the small calculated charge derived from thermoionic emission in this work. If we consider that the charge exists not only on the first layer but in all layers, then there is a large change in potential arise, whose width is proportional to hole size. The amount of the potential gradient depends on the charge. The symmetry of the potential distribution is affected by the boundary condition, while the value of the potential is proportional to it.

References

[1] Hoar, H., **"Physics of Laser Driven Plasmas"**, John Wiley & Sons (NY), 1981.

[2] Salcedo, A. et al., *"Studies of stimulated Raman scattering in laser plasma interactions"*, *Private communications*, 2002.

[3] Borghesi, M. et al., *Phys. Rev. E*, 54(6) (1996) 6769-6773.

[4] Gizzi, L.A. et al., *Laser and Particle Beams*, 19 (2001) 181-186.

[5] Galemberti, M. et al., *Laser and Particle Beams*, 19 (2001) 47-53.

[6] Borghesi, M. et al., *Phys. Rev. Lett.*, 88(13) (2002) 1- 4.

[7] Borghesi, M. et al., *Phys. of Plasma*, 9(5) (2002) 2214-2220.

[8] Tomassini, P. et al., *Phys. of Plasma*, 10(4) (2003) 917-920.

[9] Miyamoto, K., **"Fundamentals of Plasma Physics and Controlled Fusion"**, University of Tokyo (Japan), 2000.

[10] Rytter, M., *"A study of the production and characterization of a laser generated soft x-ray source"*, M.Sc. thesis, University of Southern Denmark (Denmark, 2003).

[11] Van de Sande, M.J., *"Laser scattering on low temperature plasmas High resolution and stray light rejection"*, Ph.D. thesis, Technical University of Eindhoven (Netherlands, 2002).

[12] Jonkers, J., Bakker, M. and van der Mullen, J.A.M., *J. Phys. D: Appl. Phys.*, 30 (1997) 1928.

[13] "*Numerical Solution of the Transient Diffusion Equation using the Finite Difference Method*", report at www.research.ibm.com/jourrnal/rd/444/jordansweet.html

[14] Eliasson, B., *"Numerical of Vlasov-Maxwell Modeling of Space Plasma"*, Ph.D. Thesis, 2002, Uppsala University, Sweden.

[15] "*Finite Difference Technique*", report at www.research.ibm.com/jourrnal/rd/444/jordansweet.html

[16] Abed, A.-H.M., *"Effect of plasma on the efficiency of laser machining (drilling)"*, M.Sc. thesis, University of Technology, Baghdad (1984).

[17] Ali, S.M., *"Laser-Plasma Interaction"*, M.Sc. thesis, University of Technology, Baghdad (1992).

[18] Essam, M.B., *"The electrical nature of the medium generated from laser-material interaction"*, M.Sc. thesis, University of Technology, Baghdad (1994).

[19] Mubarak, T.H., *"The transmission of laser through the interaction region with materials at different pressures and gases"*,

M.Sc. thesis, University of Technology, Baghdad (1984).
[20] Al-Qaisy, S.Q., *"Studying the surface charge resulted from plasma generated from its interaction with laser"*, M.Sc. thesis, University of Technology, Baghdad (1995).
[21] Aseel, M., *"Study into thermal effect of laser interaction with solid surface"*, M.Sc. thesis, University of Technology, Baghdad (2005).

Reviewing codes: AP0214/2010/01/IND, AP0214/2010/02/CHN

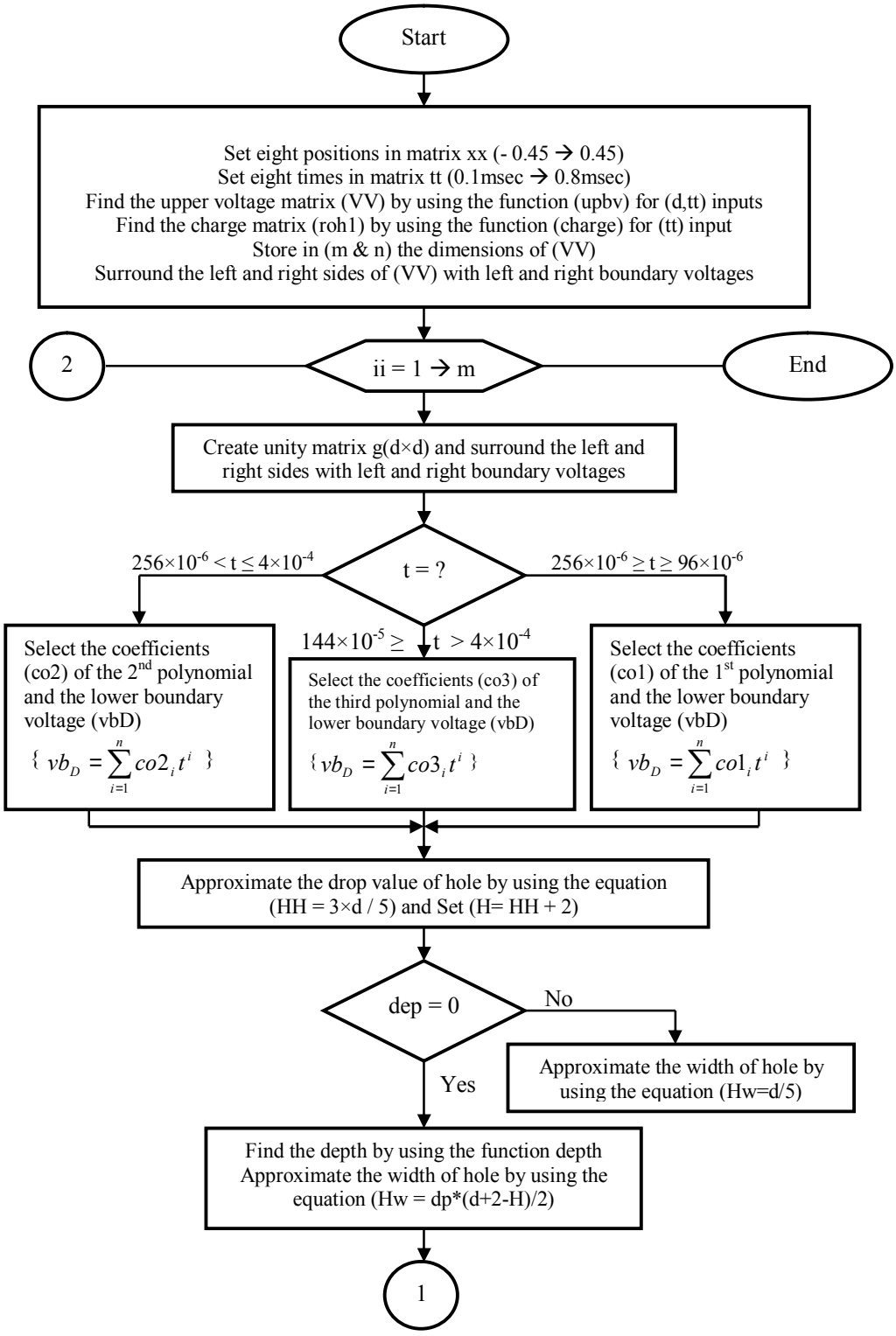

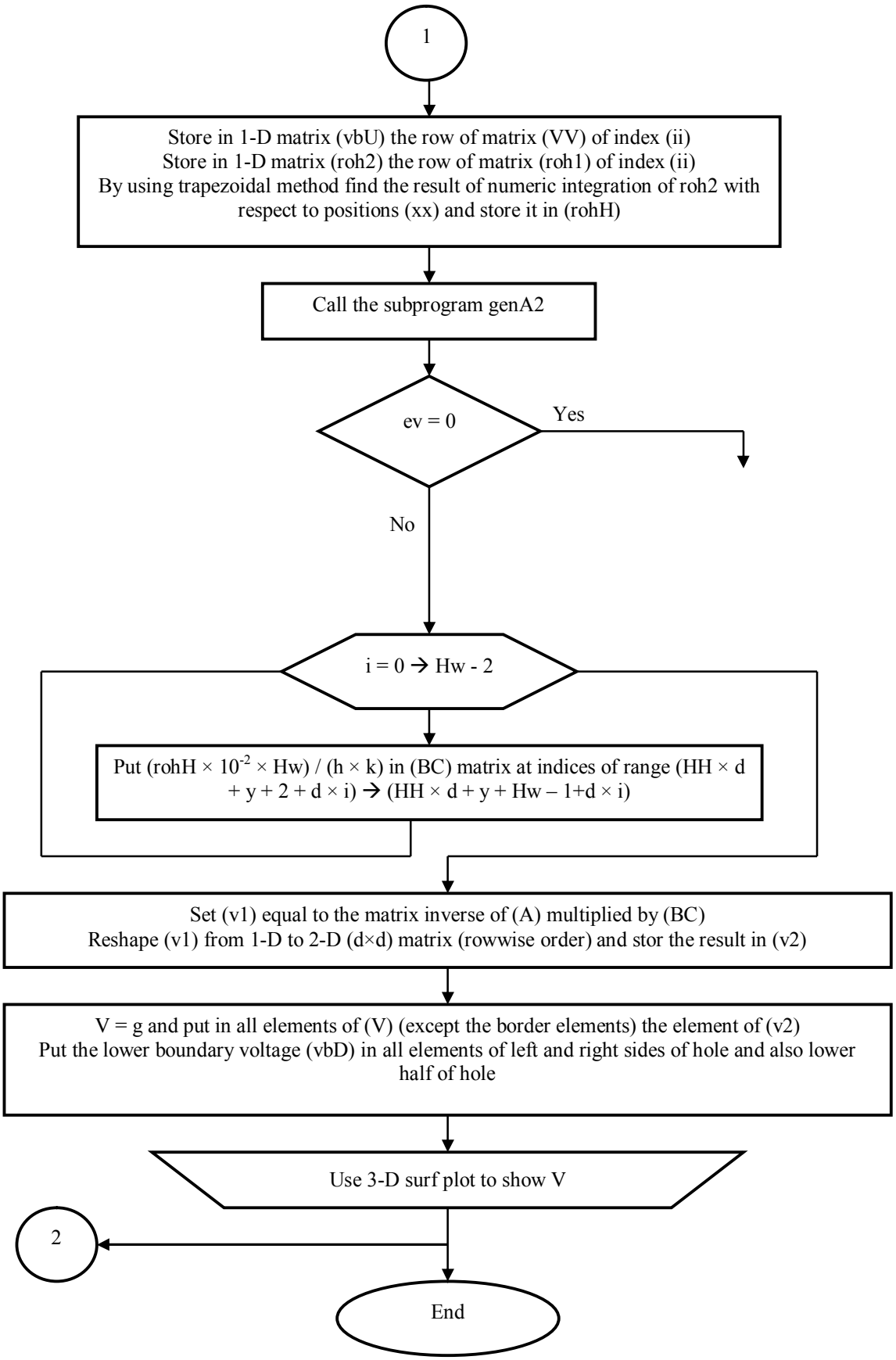

Fig. (4) Flow chart for the numerical solution of Poisson's equation

ISSN 1813-2065 Printed in IRAQ

Physicists find a big particle accelerator in the sky

Is there a giant accelerator lurking above the clouds?

The first evidence that thunderstorms can function as huge natural particle accelerators has been collected by an international team of researchers.

In a presentation at a meeting of the Royal Astronomical Society in Glasgow earlier this week, Martin Füllekrug of Bath University described how the team detected radio waves coinciding with the appearance of "sprites" – glowing orbs that occasionally flicker into existence above thunderstorms. The radio waves suggest the sprites can accelerate nearby electrons, creating a beam with the same power as a small nuclear power plant.

"The discovery of the particle accelerator allows [one] to apply the knowledge gained in particle physics to the real world, and put the expected consequences to experimental testing," Füllekrug told *physicsworld.com*.

An old idea

The idea of natural particle accelerators existing just kilometres above our heads first came in 1925, when the UK physicist and Nobel laureate Charles Wilson investigated the effects of a thundercloud's electric field. Wilson claimed that the electric field would cause an electrical breakdown of the Earth's atmosphere above the cloud, leading to transient phenomena such as sprites.

These sprites, physicists suggested, would do more than just light up the sky. As highly energetic particles or "cosmic rays" from space bombard our atmosphere, they strip air molecules of their outer electrons. In the presence of a sprite's electric field, these electrons could be forced upward in a narrow beam from the troposphere to near-Earth space. Moreover, the changing electron current would, via Maxwell's equations, produce electromagnetic waves in the radio-frequency range.

In 1998 Füllekrug's colleague Robert Roussel-Dupré of Los Alamos National Laboratory in New Mexico, US, used a supercomputer to simulate these radio waves. The simulations predicted they would come in pulses with a fairly flat spectrum – contrary to the electromagnetic spectrum of the lightning itself, which increases at lower frequencies.

Predictions confirmed

In 2008, while a group of European scientists timed the arrival of sprites from a mountain top in the French Pyrenées, Füllekrug was on the ground with a purpose-built radio-wave detector. The signals he detected coincided with the sprites and matched the characteristics of Roussel-Dupré's predictions.

"It's intriguing to see that nature creates particle accelerators just a few miles above our heads," says Füllekrug, adding: "They provide a fascinating example of the interaction between the Earth and the wider universe."

Füllekrug notes that he has no particular applications in mind for a sky-based particle accelerator, although he believes there may be wider implications for science. Researchers have many questions about the middle atmosphere because it is so difficult to set up observational platforms there. But by employing what physicists have learned about how such electron beams interact with matter, researchers could use this phenomenon to study this part of the atmosphere.

Indeed, we might be hearing a lot more about natural particle accelerators in the near future. The IBUKI satellite from Japan is currently looking at the movement of charged particles in the atmosphere. In the next few years several missions – including CHIBIS from Russia and TARANIS from France – should provide more data about these accelerators.

Curvelet-Based Optical Flow Estimation Algorithm Based on Central Derivatives

Atheer A. Sabri

Department of Electrical and Electronic Engineering, University of Technology, Baghdad, Iraq
atheeralaa@yahoo.com

Optical flow estimation is still one of the key problems in computer vision. When estimating the displacement field between two images, it is applied as soon as correspondences between pixels are needed. Some framelet-based optical flow estimation approaches has been proposed. The relatively new field of framelet shows promise in removing some of the limitations of wavelets and multiwavelets. Framelets offer more design options and hence can combine all desirable transform features. The choice of the transform is an important tool in optical flow estimation.

An approach is developed for computing optical flow in the differential framework for global models. This is achieved using schemes for the computation of the derivative using 4-point central differences filter. The proposed algorithm is compared with the most recent algorithm that is based on multiwavelet and it is found that the proposed algorithm is better than that based on multiwavelet in terms of results and required execution time. The algorithm developed in this paper is performed using MATLAB version 7 and implemented on Pentium 4, 1.7 GHz, 256 Mbyte RAM computer.

Keywords: Optical flow estimation, Curvelet transform, Central derivatives, Pre-smoothing
Received: 01 March 2010, **Revised**: 09 May 2010, **Accepted**: 16 May 2010

1. Introduction

Optical flow is a representation of the instantaneous motion of intensity points in a sequence of images. Since 1980, considerable attention has been devoted to accurately estimating the optical flow given a sequence of images. There are two main methods for computing optical flow: gradient methods and correlation methods. Apart from these, other known methods involve the statistical estimation of motion parameters [1] and the use of phase information [2]. Hayton [3] illustrates the relationship between optical flow and image registration methods, surveying the use of non-rigid correlations, mutual information, and multi-scale methods.

Suppose $I(x,t)$ is the image intensity function returning the pixel grey value at location x of the image at time t. Gradient-based methods are based on the intensity conservation assumption

$$I(x,t) = I(x + \delta x, t + \delta t) \quad (1)$$

which can be expanded in a Taylor series neglecting higher order terms [4]. In general gradient-based methods are accurate only when this assumption holds, and when frame-to-frame displacements due to motion are a fraction of a pixel so that the Taylor series approximation is meaningful. There are also problems with accuracy in determining second order derivatives due to the sensitivity of numerical integration. In practice, gradient-based methods require iteration to reduce the error and need to be augmented by a subsequent process of smoothing the resulting flow vectors over a larger image region. The need to take into account flow information over a large image region for smoothing, together with the need to cope with large displacements, has led to gradient-based approaches being supplemented by hierarchical, coarse-to-fine resolution searches, in which a first approximation to image motion is estimated using a coarse grid, and then using this information to define finer grids to limit the area in which displacements are found [5]. Another approach is to apply anisotropic smoothing, so that flow vectors are not smoothed across motion boundaries.

Correlation-based methods have been useful in sequences where the assumptions required for gradient-based methods do not apply, for example in cloud [6] and combustion[7] images. Such methods try to establish correspondences between invariant features between frames. Typical features might be blobs, corners, and edges. Alternatively, patches of the image itself may be used directly as templates to be matched in subsequent images. The main difficulties with correspondence-based methods are the uncertainty in finding invariant features due to distortion of the image, and the uncertainty in finding corresponding features. Again the spurious results obtained due to this uncertainty need to be removed or smoothed.

While the correlation surface computed by correlation-based methods is intrinsically multi-

modal, and thus capable of representing multiple motions, gradient methods assume that locally there is only one coherent motion, and they attempt to find the best values for certain parameters that describe the motion. Such single-motion methods are unreliable near motion contrast borders because the best value amounts to the mean of the various velocities present. As the surveys referred to above have shown, this is almost never the correct response. Instead, one can consider distributed representations of optical flow.

In 1980-1981, Horn and Schunck [8] devised a simple way to compute the optical flow based on regularization. It is based on the observation that the flow velocity has two components and that the basic equation for the rate of change of image brightness provides only one constraint. It is also possible to combine gradients constraints locally by assuming that the motion within a patch is constant. Early work using local combination of constraints was performed by Lucas and Kanade [9]. In 1987, Nagel [10] introduced an oriented smoothness constraint that depends on the second order derivative. In 1989, the first matching technique is reported by Anandan [11]. This method is based on a Laplacian pyramid and a course to-fine SSD-based matching strategy. Fleet and Jepson [12] use a set of velocity tuned filters and the phase behavior of the filter outputs. They claim that phase-based techniques are more robust than techniques based on conservation of intensity, especially in the presence of noise, brightness change and non-translational motion.

In 1994, Weber and Malik [13] convolve the image sequence with a set of linear separable spatiotemporal filters to produce a set of images and apply the brightness constant to these, which result in an overdetermined system of equations for the optical flow at each pixel. In 2000, Wu et al.[14] used wavelets to model flow vectors and proposed a coarse-to-fine hierarchy to reconstruct these vectors. In 2003, Bruhn et. al. [15] consider the CLG (combining of local and global) method, a recent variational technique that combines the quality of the dense flow fields of the Horn and Shunck approach with the noise robustness of the Lucas and Kanade method.

2. Optical Flow

The optical flow is a velocity field associated with brightness changes in the image. This suggests an assumption often made in methods for optical flow estimation, the brightness conservation assumption, which states that brightness of an image of any point on the object is invariant under motion.

An image intensity function is denoted by $I(x,y,t)$, and the velocity of an image pixel $m=[x,y]^T$ is [16]:

$$v_m = \dot{m} = \begin{bmatrix} u & v \end{bmatrix}^T = \begin{bmatrix} v_x & v_y \end{bmatrix}^T = \begin{bmatrix} dx/dt \\ dy/dt \end{bmatrix} \quad (2)$$

In order to compute image velocity, one must first decide which property of the image to track from one time to the next. One common, successful approach in machine vision is based on the assumption that the light reflected from an object surface remains constant through time, in which case one can track points of constant image intensity. The initial hypothesis in measuring image motion is that the intensity structures of local time varying image regions are approximately constant under motion for at least a short duration (dt), i.e. [17,18]:

$$I(x+u\,dt, y+v\,dt, t+dt) = I(x,y,t) \quad (3)$$

If the brightness changes smoothly with x, y and t, the left-hand-side is expanded by Taylor series as follows:

$$I(x,y,t) + \frac{\partial I}{\partial x}udt + \frac{\partial I}{\partial y}vdt + \frac{\partial I}{\partial t}dt + O(dt^2) = I(x,y,t) \quad (4)$$

By neglecting higher order derivative $O(dt^2)$:

$$\frac{\partial I}{\partial x}u + \frac{\partial I}{\partial y}v + \frac{\partial I}{\partial t} = 0 \quad (5)$$

i.e.,

$$\nabla I.v_m + \frac{\partial I}{\partial t} = 0 \quad (6)$$

where

$\nabla I = \left[\frac{\partial I}{\partial x}, \frac{\partial I}{\partial y}\right]^T$ is image gradient at pixel m, which can be obtained from images

3. Curvelet Transform

The new curvelet transform is developed over several years in an attempt to break an inherent limit plaguing wavelet transform. This limit arises from the well-known and frequently depicted fact that the two-dimensional wavelet transform of images exhibits large wavelet coefficients even at fine scales, all along the important edges in the image, so that in a map of the large wavelet coefficients one sees the edges of the images repeated at scale after scale. While this effect is visually interesting, it means that many wavelet coefficients are required in order to reconstruct the edges in an image properly. With so many coefficients to estimate, denoising faces certain difficulties. There is, owing to well-known statistical principles, an imposing tradeoff between parsimony and accuracy which even in the best balancing leads to a relatively high Mean Squared Error (MSE) [19].

While this tradeoff is intrinsic to wavelet methods (and also to Fourier and many other standard methods), there exist, on theoretical grounds, better de-noising schemes for

recovering images which are smooth away from edges. For example, asymptotic arguments show that, in a certain continuum model of treating noisy images with formal noise parameter ε, for recovering an image which is C^2 smooth away from C^2 edges, the ideal MSE scales like $\varepsilon^{4/3}$ whereas the MSE acheivable by wavelet methods scales only like ε [20]).

To approach this ideal MSE, one should develop new expansions which accurately represent smooth functions using only a few nonzero coefficients, and which also accurately represent edges using only a few nonzero coefficients. Then, because so few coefficients are required either for the smooth parts or the edge parts, the balance between parsimony and accuracy will be much more favorable and a lower MSE results. The curvelet transform is developed explicitly to show that this combined sparsity in representation of both smooth functions and edges is possible [19].

So according to theory for a certain continuous-space model, discrete curvelet transforms provide near-ideal sparsity of representation of both smooth objects and of objects with edges. In a certain continuous-space statistical theory, this implies that simple thresholding of noisy coefficients in these expansions is a near-optimal method of de-noising in the presence of white Gaussian noise [19].

Curvelets are interesting because they efficiently address very important problems where wavelet ideas are far from ideal. We give three examples [21]:

3.1. *Optimally sparse representation of objects with edges*

Curvelets provide optimally sparse representations of objects which display curve-punctuated smoothness except for discontinuity along a general curve with bounded curvature. Such representations are nearly as sparse as if the object were not singular and turn out to be far more sparse than the wavelet decomposition of the object.

This phenomenon has immediate applications in approximation theory and in statistical estimation. In approximation theory, let f_m be the m-term curvelet approximation (corresponding to the m largest coefficients in the curvelet series) to an object $f(x_1,x_2) \in L^2(R^2)$. Then the enhanced sparsity says that if the object f is singular along a generic smooth C^2 curve but otherwise smooth, the approximation error obeys

$$\|f - f_m\|_{L^2}^2 \le C.(\log m)^3.m^{-2} \qquad (7)$$

and is optimal in the sense that no other representation can yield a smaller asymptotic error with the same number of terms. The implication in statistics is that one can recover such objects from noisy data by simple curvelet shrinkage and obtain a Mean Squared Error (MSE) order of magnitude better than what is achieved by more traditional methods. In fact, the recovery is provably asymptotically near-optimal. The statistical optimality of the curvelet shrinkage extends to other situations involving indirect measurements as in a large class of ill-posed inverse problems [22].

3.2. *Optimal image reconstruction in severely ill-posed problems*

Curvelets also have special microlocal features which make them especially adapted to certain reconstruction problems with missing data. For example, in many important medical applications, one wishes to reconstruct an object $f(x_1,x_2)$ from noisy and incomplete tomographic data [23], i.e., a subset of line integrals of f corrupted by additive noise modeling uncertainty in the measurements.

Because of its relevance in biomedical imaging, this problem has been extensively studied (compare the vast literature on computed tomography). Yet, curvelets offer surprisingly new quantitative insights [24]. For example, a beautiful application of the phase-space localization of the curvelet transform allows a very precise description of those features of the object of f which can be reconstructed accurately from such data and how well, and of those features which cannot be recovered. Roughly speaking, the data acquisition geometry separates the curvelet expansion of the object into two pieces

$$f = \sum_{n \in Good} \langle f, \Phi_n \rangle \Phi_n + \sum_{n \notin Good} \langle f, \Phi_n \rangle \Phi_n \qquad (8)$$

The first part of the expansion can be recovered accurately while the second part cannot. What is interesting here is that one can provably reconstruct the "recoverable" part with an accuracy similar to that one would achieve even if one had complete data. There is indeed a quantitative theory showing that for some statistical models which allow for discontinuities in the object to be recovered, there are simple algorithms based on the shrinkage of curvelet-biorthogonal decompositions, which achieve optimal statistical rates of convergence; that is, such that there are no other estimating procedure which, in an asymptotic sense, give fundamentally better MSEs [21,24].

4. The Proposed Algorithm

A new algorithm for computing optical flow in the differential framework is proposed here. This algorithm is performed comparably to the Horn and Schunck approach but with a higher

 ISSN 1813-2065 Printed in IRAQ

density of estimates. The proposed algorithm is as follows:

1) Pre-smoothing using 2D Discrete Curvelet Transform (DCvT)

A 2D discrete curvelet transform is used to perform pre-smoothing. This is done to reduce noise and aliasing.

2) Calculate the Partial Derivative

A four point central difference is employed. This is done with a size five kernel with taps

$$\frac{1}{12}[-1,8,0,-8,1] \quad (9)$$

which require five input images, allowing two pixels on either side of the central pixel to be included in the differencing.

3) Initialize $u(x,y)$ *and* $v(x,y)$ *for all* (x,y) *pixel*.

4) Compute Velocities

Calculate the following steps iteratively and for each iteration perform the following steps:

- Initialize $u_{x,y}$ and $v_{x,y}$ for all (x,y) pixel.
- Calculate the Laplacian of the flow velocities:

The Laplacian of u and v, $\nabla^2 u$ and $\nabla^2 v$, can be obtained by applying a 3×3 window operator to each point in the u and v planes. The 3×3 window operator is shown in Fig. (1)

$(x-1,y-1)$	$(x-1,y)$	$(x-1,y+1)$
$(x,y-1)$	(x,y)	$(x,y+1)$
$(x+1,y-1)$	$(x+1,y)$	$(x+1,y+1)$

1/12	1/6	1/12
1/6	-1	1/6
1/12	1/6	1/12

Fig. (1) a 3×3 window operator

- Apply Gauss Seidel method to find a new set of velocity estimates

$$u^{k+1} = \bar{u}^k - \frac{I_x\left[I_x\bar{u}^k + I_y\bar{v}^k + I_t\right]}{\lambda^2 + I_x^2 + I_y^2} \quad (10)$$

$$v^{k+1} = \bar{v}^k - \frac{I_y\left[I_x u^k + I_y v^k + I_t\right]}{\lambda^2 + I_x^2 + I_y^2} \quad (11)$$

5) Threshold the Estimated Velocities on the basis of spatial intensity gradient as follows:

$$\left(u_{x,y}, v_{x,y}\right) = \begin{cases} 0 & if \quad M(x,y) < \tau \\ \left(u_{x,y}, v_{x,y}\right) & if \quad M(x,y) > \tau \end{cases} \quad (12)$$

where $M(x,y) = \|\nabla I(x,y)\| = \sqrt{I_x^2 + I_y^2}$

The proposed algorithm is shown in Fig (2).

5. Experimental Results

The proposed algorithm presented in this paper is tested to estimate the optical flow on the following image sequences:

Translating square: A simple example is tested as shown in Fig. (3), which is a translating dark square translating in a bright background.

SRI Sequence: In this sequence a camera translates parallel to the ground plane, perpendicular to its line of sight, and in front of a cluster of trees. The estimated optical flow using the proposed algorithm is shown in Fig. (4).

Hamburg Taxi Sequence: In this sequence there are four moving objects which are: A taxi turning the corner, a car in the lower left (driving from left to right), a van in the lower right driving from right to left, and finally pedestrian in the upper left. The estimated optical flow is shown in Fig. (5).

Rotating Rubic's Cube: In this image, a Rubic's cube is rotating counterclockwise on a turntable. The estimated optical flow is shown in Fig. (6).

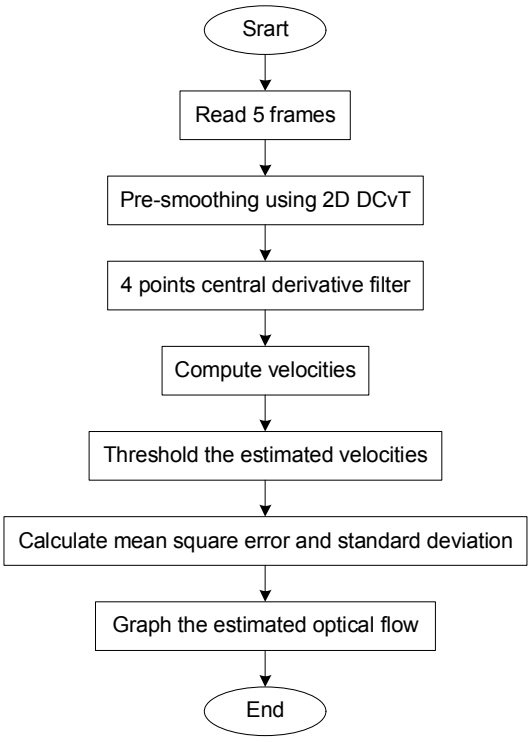

Fig. (2) The Flowchart of the Proposed Algorithm

6. Conclusions and Discussions

The proposed algorithm here is implemented using MATLAB package version 7 on Pentium4/1.7GHz processor, 80GB hard disk with 512MB RAM. From the obtained results, it can be concluded that curvelet transform gives good results for the estimated optical flow. Finally to find the benefit of this algorithm, now this algorithm is compared with the algorithm presented in [18]. The work presented in [18] is

the same as proposed in this paper except it has been used 2D Multiwavelet transform instead of 2D curvelet transform. Table (1) presents a comparison between the two works. It can be concluded from Table (1) that the proposed algorithm in this paper is better than presented in [18]. Also from Table (2), which gives us the time required to execute each algorithm, it can be concluded that the proposed algorithm is much faster than the work presented in [18]. The main reason for that is curvelets can find estimates also on curves that multiwavelets can not find well.

Table (1) A comparison between the proposed algorithm and the work in [18]

Sequence	The Proposed Algorithm		Work presented in [18]	
	Mean Error	Standard Deviation	Mean Error	Standard Deviation
Translating Square	0.0671	2.8105	0.0725	3.7221
SRI Sequence	0.1168	1.8955	0.2688	3.8662
Hamburg Taxi	0.1685	1.4426	0.6344	5.6853
Rotating Rubic's Cube	0.1870	0.8432	0.4849	5.6933

Table (2) The time required to execute the proposed algorithm and the work in [10]

Sequence	The Proposed Algorithm (sec)	The work presented in [18] (sec)
Translating Square	4.9220	5.7960
SRI Sequence	11.0630	39.0940
Hamburg Taxi	11.9380	37.7970
Rotating Rubic's Cube	10.8130	40.9840

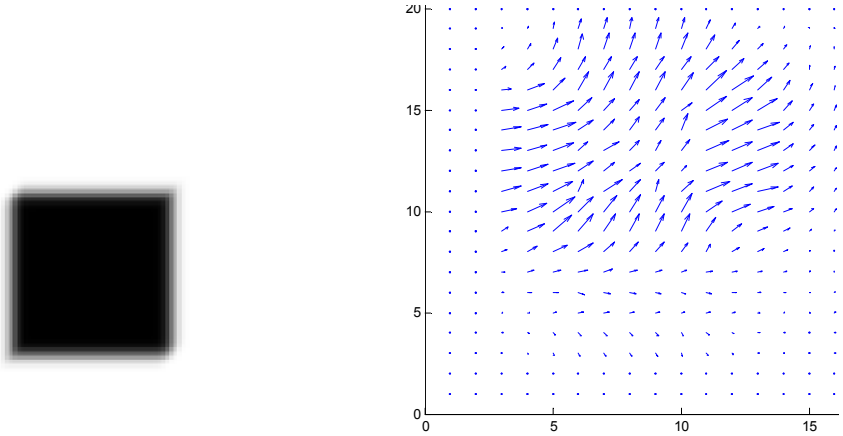

Fig. (3) The translating square and its estimated optical flow

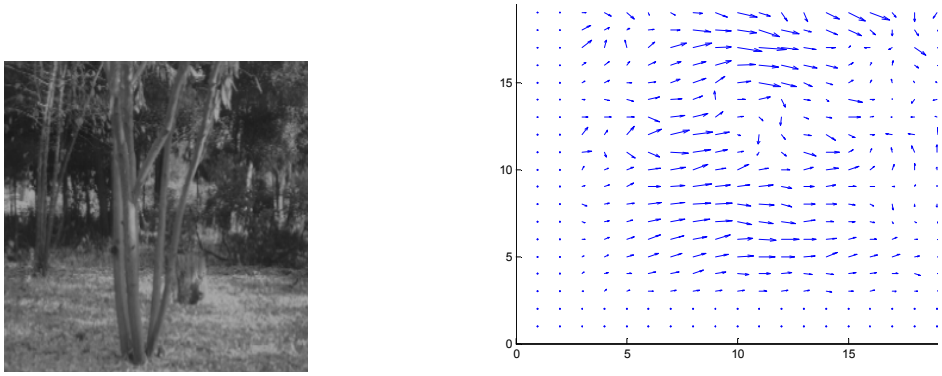

Fig. (4) The SRI sequence and its estimated optical flow

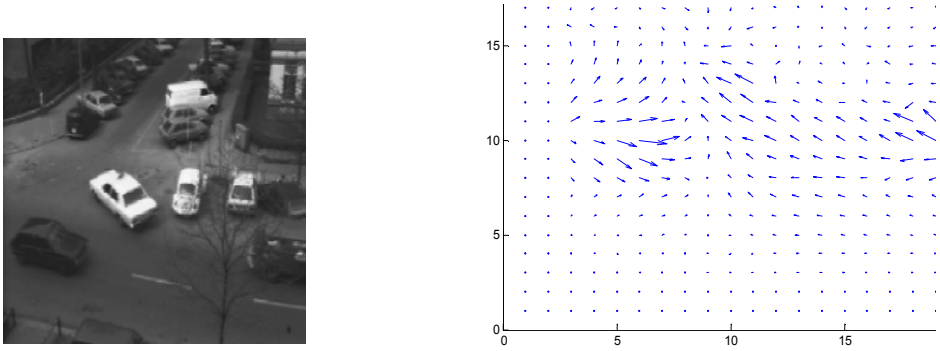

Fig. (5) The Hamburg Taxi image and its estimated optical flow

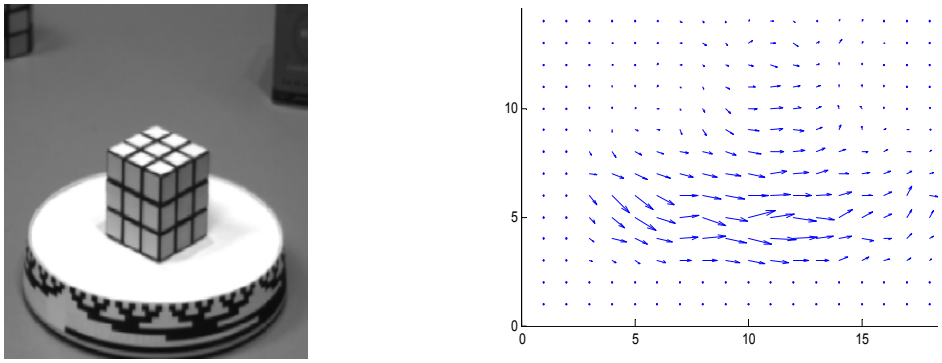

Fig. (6) The Rotating Cube and its estimated optical flow

References

[1] C.M. Fan, N.M. Namazi and P.B. Penafiel, *IEEE Trans. on Pattern Analysis and Machine Intelligence,* 18(3) (1996) 348-352.

[2] D.J. Fleet and A.D. Jepson, *Int. J. of Computer Vision* 5(1) (1990) 77-104.

[3] P.M. Hayton et al., *Artif. Intellig.,* 114 (1999) 125-156.

[4] B.K.P. Horn and B.G. Schunck, *Artif. Intellig.,* 17 (1981) 185-204.

[5] R. Battiti, E Amaldi and C. Koch, *Int. J. of Computer Vision* 6(2) (1991) 133-145.

[6] Q.X. Wu, *IEEE Trans. on Pattern Anal. and Machine Intelligence*, 17(8) (1995) 843-853.

[7] J.H. Sun, D.A. Yates and D.E. Winterbone, *Experiments in Fluids,* 20 (1996) 335-345.

[8] B.K.P. Horn and B.G. Schunck, *Artif. Intellig.*, 17 (1981) 185-204.

[9] B.D. Lucas and T. Kanade, "An Iterative Image Registration Technique with an Application to Stereo vision", *Proc. of Imaging Workshop*, 1981.

[10] H. Nagel, *Artif. Intellig.,* 33 (1987) 29-32.

[11] P. Anandan, Int. J. of Computer Vision, 2 (1989) 283-310.

[12] D.J. Fleet and A.D. Jepson, Int. J. of Computer Vision, 5 (1) (1990) 77-104.

[13] J. Weber and J. Malik, Int. J. of Computer Vision, 14 (1) (1995) 67-81.

[14] Y.T. Wu et al., Int. J. of Computer Vision, 38(2) (2000) 129–152.

[15] A. Bruhn et al., "Real-Time Optic Flow Computation with Variational Methods", Computer Analysis of Images and Patterns (CAIP), Book, Lecture Notes in Computer Science (LNCS) 2756 (2003) 222-229.

[16] Y. Wu, "Optical Flow and Motion Analysis", Computer Vision Notes, www.ece.northweastern.edu.

[17] R.P. Rao, B.A. Olshausen and M.S. Lewicki, **"Probabilistic Models of the Brain: Perception and Neural Function"**, MIT Press (2001) 80-100.

[18] H.N. Al-Taai, "Computationally-Efficient Wavelet-Based Algorithms for Optical Flow Estimation", Ph.D. thesis, University of Technology, Baghdad, Iraq (2005).

[19] J.L. Starck, E.J. Candès and D.L. Donoho, *IEEE Trans. on Image Process.*, 11(6) (2002) 670-684.

[20] E.J. Candès and D.L. Donoho, "Edge-preserving denoising in linear inverse problems: Optimality of curvelet frames", Technical report, Stanford University (2000).

[21] E.J. Candès et al., "Fast Discrete Curvelet Transforms", Technical Report, Caltech (2005).

[22] E.J. Candès and D. L. Donoho, *Commun. on Pure and Appl. Math*, 67(2) (2004) 219–266.

[23] F. Natterer, **"The mathematics of computerized tomography"**, B.G. Teubner, John-Wiley & Sons (1986).

[24] E.J. Candes and D.L. Donoho, "Curvelets: new tools for limited-angle tomography", Technical report, California Institute of Technology (2004).

Reviewing codes: AP0186/2010/01/TWN, AP0186/2010/02/IND

Design and Analysis of Special Small Size Cross Dipole Antenna

Fawwaz J. Jibrael

Department of Electrical and Electronic Engineering, University of Technology, Baghdad, IRAQ

In this paper, a crossed dipole antenna combined with the quadratic Koch curve geometry, which has a novel configuration, is proposed and investigated for low profile and multi-band performance in communication systems. The proposed antenna has operating frequencies of 1.543GHz, 2.537GHz, 3.038GHz, 3.469GHz and 3.769GHz. The field pattern of the proposed antenna is described and simulated in the three planes: XZ-plane, YZ-plane, and XY-plane. The radiation characteristics, VSWR, reflection coefficients, and input impedance of the proposed antenna are described and simulated using the 4NEC software package.

Keywords: Fractal geometry, Multi-band antenna, Koch curve, Dipole antenna
Received: 25 April 2010, **Revised**: 04 May 2010, **Accepted**: 11 June 2010

1. Introduction

For the current world of wireless communications, it has required compact and wider bandwidth antennas. Recent progress in the study of fractal antennas suggests some attractive solutions of using a single small antenna operating in several frequency bands [1]. Fractals are a class of shapes which have no characteristic size. Each fractal is composed of multiple iterations of a single elementary shape. The iterations can continue infinitely, thus forming a shape within a finite boundary but of infinite length or area. This indicates fractal shapes are compact, meaning that they can occupy a portion of space more efficiently than other antenna types. In previously published literature [2-3], it has been discovered that fractal shapes radiate electromagnetic energy well and also been demonstrated that fractal antennas exhibit compressed resonance and multi-band behavior, which can radiate signals at multiple frequency bands when their impedance properties are compared to those of Euclidean antennas, having the same overall size. Fractal antennas have also been shown to exhibit lower resonant frequencies than Euclidean antennas of the same overall size. All the properties discovered, fractal shapes are advantageous over traditional antenna types, which can be helpful in applications requiring reduced size antennas, like mobile wireless communication because smaller receivers could be produced.

In modern terminal antenna technology, there is an increasing need for singly-fed antennas operating in more than two frequency bands. Fractal antennas have been demonstrated to enhance antenna properties due to their self-similarity behavior. Multi-band behavior for Koch monopole and dipole are fully demonstrated in [4]. This paper presents the complete design and simulations of the quadratic Koch curve multi-band cross-dipole antenna that results from combining the normal cross-dipole antenna with the quadratic Koch curve geometry.

2. Proposed Antenna Geometry

Quadratic Koch curve geometry with different iterations is shown in Fig. (1) [5]. The proposed geometry includes the replacement of each arm in the normal dipole crossed antenna in Fig. (2a) with second-iteration quadratic Koch curve geometry. The proposed antenna is shown in Fig. (2b).

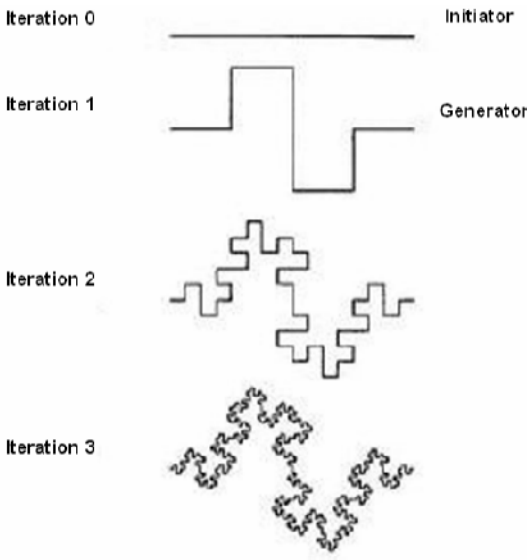

Fig. (1) First three stages of the construction of the quadratic Koch curve

3. Proposed Antenna Design and Simulation Results

In this work, method of moment simulation code (NEC) is used to perform a detailed study of VSWR, input impedance, and radiation

ISSN 1813-2065

pattern characteristics of the cross quadratic Koch dipole antenna in free space.

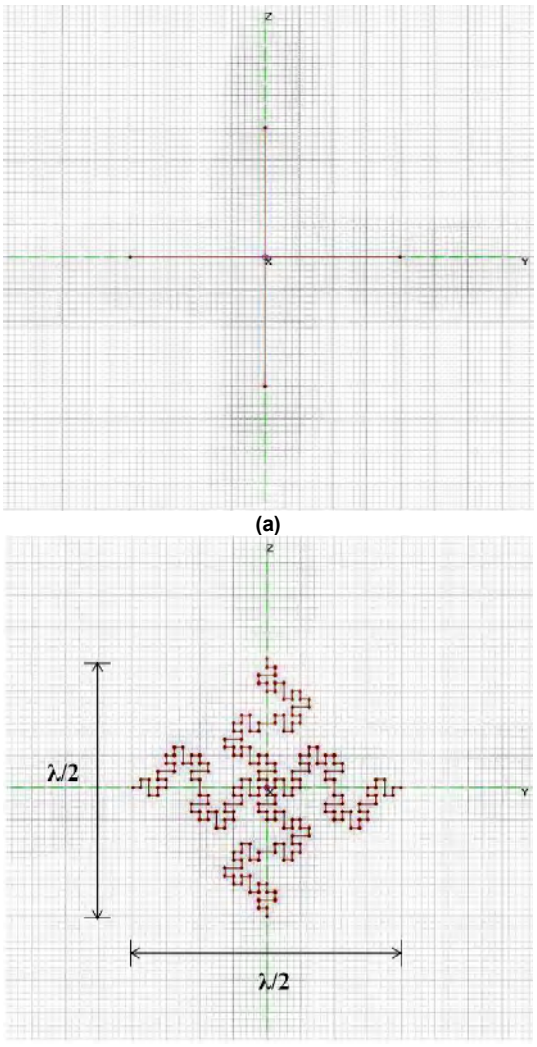

Fig. (2) Cross Dipole Antenna (a) cross normal dipole antenna (b) proposed cross dipole antenna

The NEC is a computer code based on the method of moment for analyzing the electromagnetic response of an arbitrary structure consisting of wires or surfaces, such as Hilbert and Koch curves. The Method of Moment (MoM) is used to calculate the current distribution along the cross quadratic Koch curve antenna, and hence the radiation characteristics of the antenna [6]. The modeling process is simply done by dividing all straight wires into short segments where the current in one segment is considered constant along the length of the short segment [7]. The cross fractal wire dipole antenna consists of second iteration quadratic Koch curve, as shown in Fig. (2b), and this antenna is placed in YZ-plane with design frequency equal to 750MHz. The feed source point of this antenna is placed at the origin (0,0,0), and this source is set to 1 volt. For the design frequency of 750MHz, the design wavelength, λ_0 is 0.4m (40cm) then the length of the corresponding $\lambda/2$ dipole antenna length will be of 20cm. Figure (3) shows the visualization of this dipole antenna geometry by using NEC-viewer software.

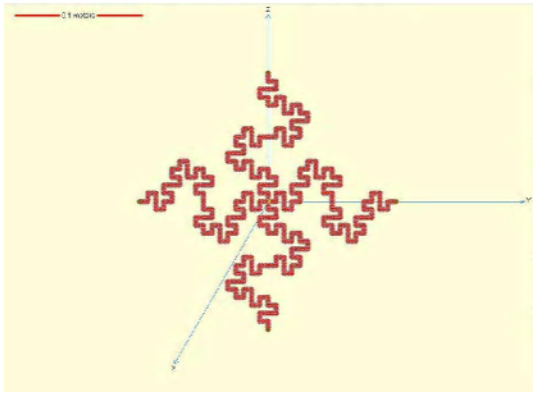

Fig. (3) Visualization of the modeled cross fractal dipole antenna geometry

The real and imaginary parts of the input impedance and the simulated 50Ω-VSWR of this proposed antenna are shown in Figs. (4) and (5) over a frequency range from 0 to 4GHz. Figures (4) and (5) shows that the antenna has several resonant frequencies with VSWR<2. The three dimensional gain radiation patterns at the resonant frequencies for the proposed antenna have been illustrated in Fig. (6).

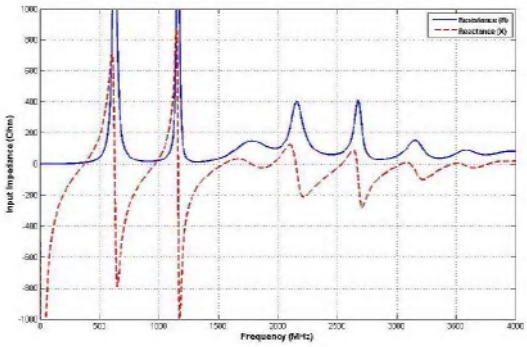

Fig. (4) Antenna input impedance

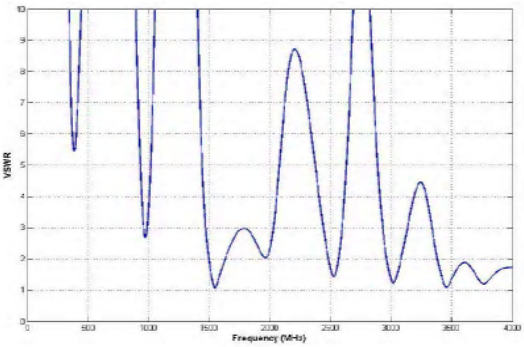

Fig. (5) Simulated 50Ω, VSWR *vs.* frequency

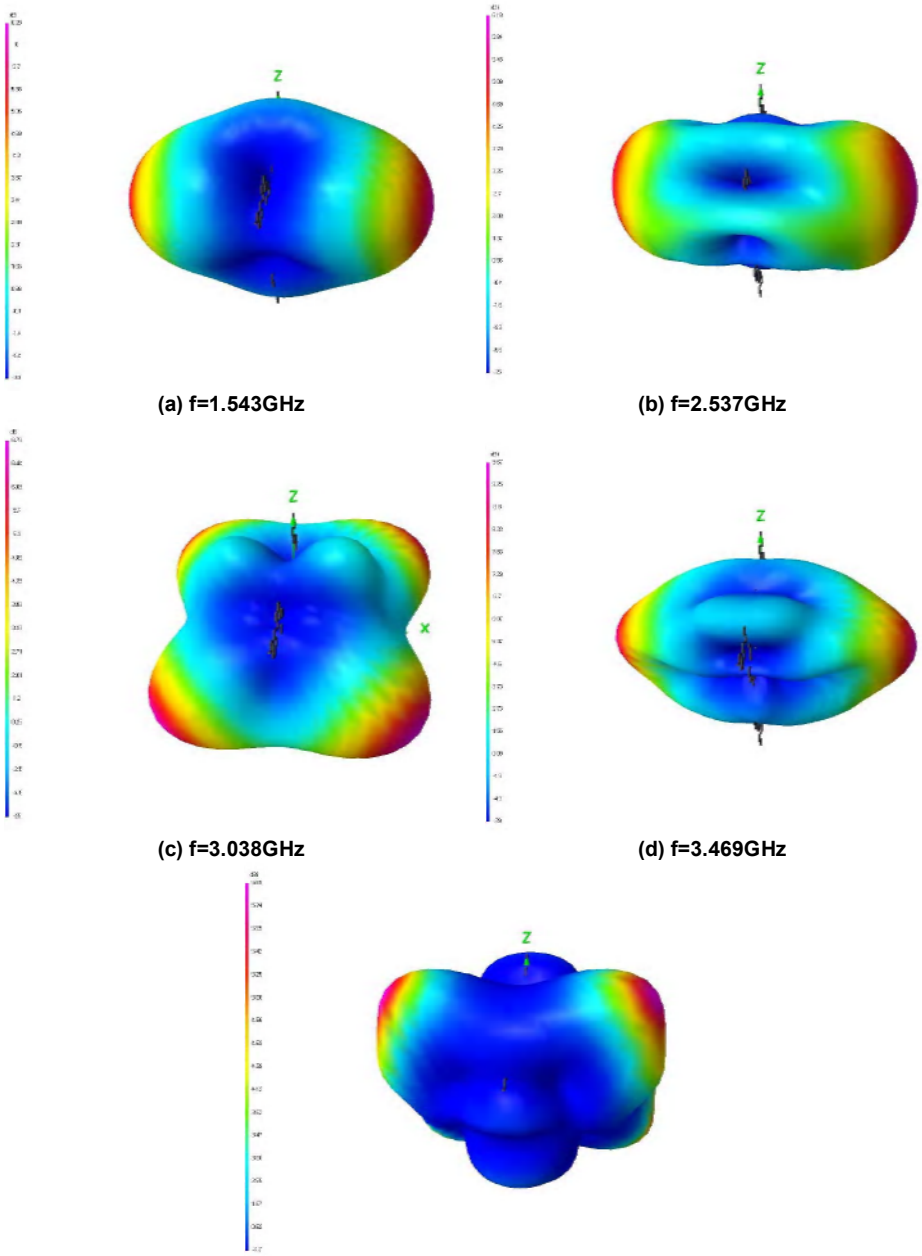

(a) f=1.543GHz (b) f=2.537GHz

(c) f=3.038GHz (d) f=3.469GHz

(e) f=3.769GHz

Fig. (6) 3D gain radiation pattern

Table (1) shows these resonant frequencies, and the corresponding input impedance of each one, with peak gain, VSWR and reflection coefficients. The radiation patterns at these resonant frequencies, in the planes YZ-plane, XZ-plane, and XY-plane are depicted in Fig. (7), where the antenna is placed in the YZ-plane.

Table (1) Simulation results of the Proposed Antenna

Frequency (GHz)	Input Impedance (Ω)		VSWR	Reflection Coefficient (dB)	Peak Gain (dB)
	R	X			
1.543	46.72	j0.215	1.07	-29.4	6.28
2.537	73.48	j0.535	1.47	-14.4	6.18
3.038	68.23	j0.122	1.365	-16.2	6.78
3.469	56.63	j0.055	1.133	-24.1	9.67
3.769	60.08	-j0.04	1.202	-20.8	5.89

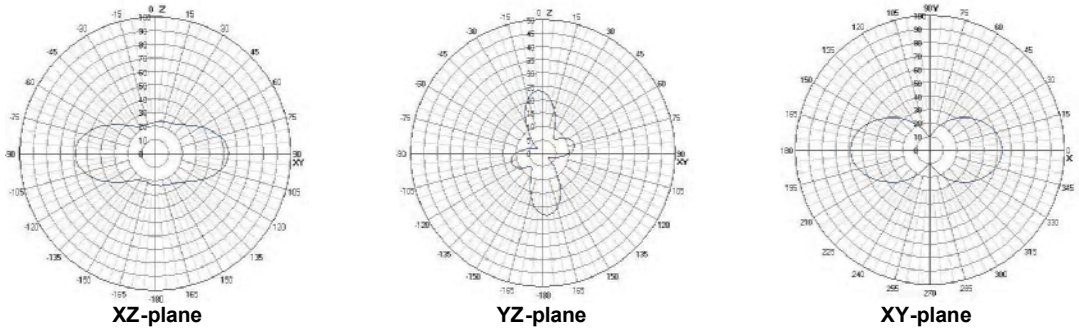

XZ-plane YZ-plane XY-plane

(a) f=1.543GHz

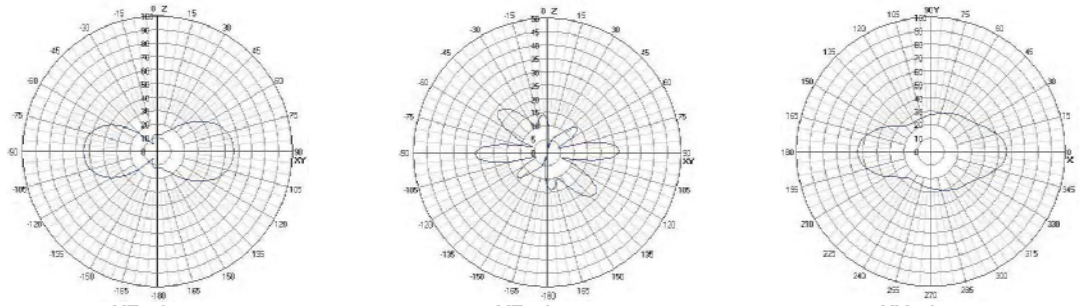

XZ-plane YZ-plane XY-plane

(b) f=2.537GHz

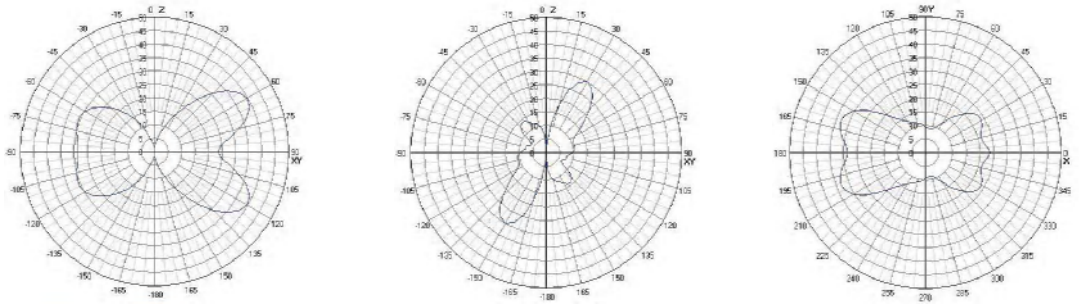

XZ-plane YZ-plane XY-plane

(c) f=3.038GHz

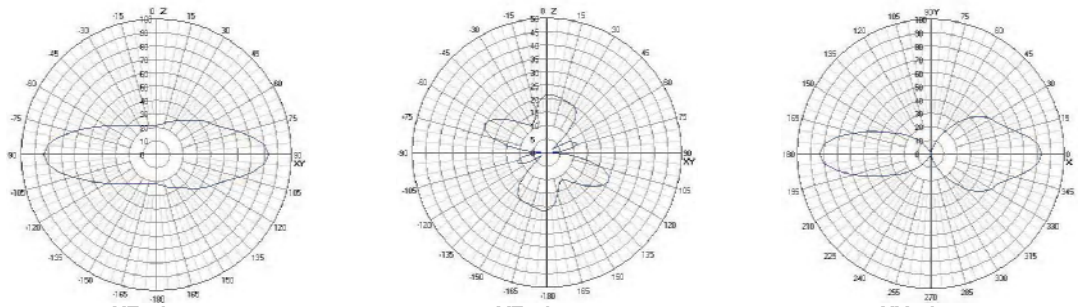

XZ-plane YZ-plane XY-plane

(d) f=3.469GHz

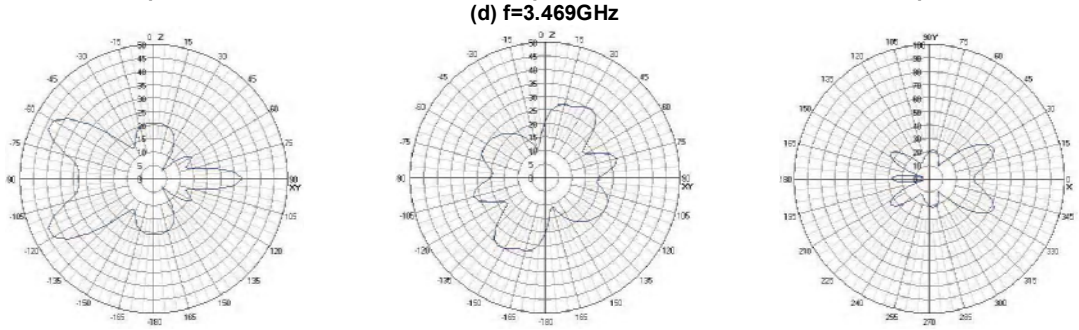

XZ-plane YZ-plane XY-plane

(e) f=3.769GHz

Fig. (7) Radiation patterns of the proposed antenna in the three planes

4. Conclusion

A novel small size multi-band cross dipole antenna based on a fractal second iteration quadratic Koch curve, has is presented. The analysis of the proposed antenna is performed using the method of moments (MOM), and the numerical simulations show that the proposed antenna has the ability to work as multi-band antenna at the frequencies 1.543 GHz, 2.537 GHz, 3.038 GHz, 3.469 GHz, and 3.769 GHz. In addition, this antenna has VSWR<2 at all aforementioned resonance frequencies. The compact size of the antenna geometry makes it useful for wireless applications.

References

[1] T. Tiehong and Z. Zheng, *Electron. Lett.*, *Proc. of ICCT* – (2003) 1907-1910.

[2] S.R. Best, "The Koch Fractal Monopole Antenna: The Significant of Fractal Geometry in Determining Antenna Performance," Technical Report, Manchester, NH, Cushcraft Corporation (2005).

[3] P. Simedra, "Design and Implementation of Compact Microstrip Fractal Antennas," Project Report, London, Ontario, The University Of Western Ontario (2004).

[4] S.H Zainud-Deen, K.H. Awadalla S.A. Khamis and N.D. El-Shalaby, "Radiation and Scattering from Koch Fractal Antennas," *21st National Radio Science Conference (NRSC)*, B8 - 1-9, March 16-18 (2004).

[5] F.J. Jibrael, H.A. Hammas and M.F. Hasan, *J. of Eng. and Appl. Sci.*, 3(4) (2008) 373-376.

[6] C. A. Balanis, **"Antenna Theory: Analysis and Design"**, 3rd ed., Wiley (2005), Ch.8, 433-495.

[7] G.J. Burke and A.J. Poggio, "Numerical Electromagnetic Code (NEC)-Program description," January, Lawrence Livermore Laboratory (1981).

Reviewing codes: AP0206/2010/01/CHN, AP0206/2010/02/GRE

SPIE *Scientific Calendar*

SPIE Laser Damage

27 - 29 September 2010
SPIE Laser Damage
Boulder, Colorado, USA

SPIE Asia-Pacific Remote Sensing

10 - 15 October 2010
SPIE Asia Pacific Remote Sensing
Incheon, Republic of Korea

SPIE LithographyAsia Korea

13 - 15 October 2010
SPIE Lithography Asia
Incheon, Republic of Korea

SPIE/COS Photonics Asia

18 - 21 October 2010
SPIE/COS Photonics Asia
Beijing, China

SPIE Photonics West

22 - 27 January 2011
EXHIBITION
25 - 27 January 2011
SPIE Photonics West
Sub-conferences
BiOS, part of Photonics West
EXHIBITION
22 - 23 January 2011
SPIE LASE, part of Photonics West
SPIE MOEMS-MEMS, part of Photonics West
SPIE OPTO, part of Photonics West
SPIE Green Photonics, part of Photonics West
San Francisco, California, USA

IS&T / SPIE Electronic Imaging SCIENCE AND TECHNOLOGY

23 - 27 January 2011
IS&T/SPIE Electronic Imaging 2011
San Francisco Airport, California, USA

SPIE Medical Imaging

12 - 17 February 2011
SPIE Medical Imaging
Lake Buena Vista (Orlando), Florida, USA

SPIE Advanced Lithography

27 February - 4 March 2011
EXHIBITION
1 - 2 March 2011
SPIE Advanced Lithography San Jose, California, USA

SPIE Smart Structures/NDE

6 - 10 March 2011
EXHIBITION
8 - 9 March 2011
SPIE Smart Structures and Materials & Nondestructive Evaluation and Health Monitoring
San Diego, California, USA

SPIE Green Photonics

28 - 31 March 2011
SPIE Green Photonics
Strasbourg, France

SPIE Defense, Security+Sensing

25 - 29 April 2011
EXHIBITION
26 - 28 April 2011
SPIE Defense, Security, and Sensing
Orlando, Florida, USA

SPIE Optifab

9 - 12 May 2011
EXHIBITION
10 - 12 May 2011
SPIE Optifab
Rochester, New York, USA

Microstructural Study of Copper-Carbon Composite Interface

Awfa A.R. Abdullah

School of Applied Sciences, University of Technology, Baghdad, Iraq

Graphite is a very attractive candidate for copper-metal matrix composites. However, copper does not wet graphite, which makes the production of copper-graphite composites difficult. Because of the strong possibilities of these combinations in forming highly desirable composites, copper-carbon composites prepared by hot uniaxial pressure were investigated. The copper-carbon interface is of the samples was examined microscopically using optical microscopy. The observed microstructure at copper interface is composed of copper-carbon interaction layer. The adhesion between copper and graphite was achieved. However, there is no intimate contact between copper and graphite film at interface. To determine the diffusion of carbon through copper matrix by X-ray diffraction was used.

Keywords: Cu–C matrix composite, Graphite composite, Wettability, Carbon diffusion
Received: 28 April 2010, **Revised**: 10 June 2010, **Accepted**: 18 June 2010

1. Introduction

Composites are very interesting and important subset of advanced materials, because they allow a designer the ability to craft new materials with property compensations superior to those of non- reinforced metals, ceramics and polymers. Generally, a composite is considered to be any multiphase material that exhibits significant properties of both constituent phases such that better properties are achieved. The principal of combined action, an often valid supposition, states that a higher level of properties can be achieved by combining two or more dissimilar materials. Most composites are created to improve the following mechanical properties: stiffness, toughness, ambient and high temperature strength [1]. The ability to combine properties is especially crucial for aerospace, underwater, and transportation applications [2]. Metal matrix Composites (MMC) is a combination of matrix and reinforcement: matrix, is a ductile metal, usually super alloys or alloys of aluminum, magnesium, titanium, and copper. The reinforcements include particulates, continuous and discontinuous fibers, and whiskers. Some of the continuous fibers are carbon, silicon carbide, boron, alumina, and refractory metals [3]. These composites materials are usually used at elevated temperatures because they are often more resistant to creep, and they exhibit lower thermal conductivity than their bulk counterparts. Graphite copper composites have tailorable properties, are useful to high temperatures in air, and provide excellent mechanical characteristics, as well as high electrical and thermal conductivity [4]. They offer easier processing as compared with steel [5]. Although the various methods for joining graphite to other metals such as mechanical fastening, arc welding, or diffusion bonding have been examined, it was shown that it is difficult to produce a sound joint without leakage [6,7]. Previous studies were achieved to investigate the interfacial interaction for MMC and its interfacial structures [8-10]. Essentially, it is impossible to braze graphite with copper filler metal because no wetting occurs [6,11].

2. Experimental Work

Materials used in this research are: copper (99.95% purity) and graphite as base materials (graphite sheets were excluded due to fracture during the hot uniaxial pressing operation) to with stand the applied pressure [12,13]. Base materials in this research were copper and graphite and examined using X-Ray Diffraction, before and after the hot uniaxial pressing operation (see Fig. (1)).

Graphite samples were cut into squares with dimensions, $14x14x5mm^3$ using a hydraulic cutting machine. One surface of the samples was wet ground using silicon carbide papers, polished with 1μm diamond paste, cleaned by alcohol, and finally cleaned ultrasonically for 10min using acetone as a medium. Copper sheets interlayer were flattened by anvil, then subjected to pickling (10% HNO_3 and distilled water) to remove oxide film, cleaned with soap and water rinsed and finally ultrasonically cleaned for 10min. using acetone bath and then dried, etching solution for copper sheets was 50ml distilled water, 150ml hydrochloric acid (specific gravity 1.19 and 36% conc.) and 25g chromium (VI) oxide for 20s. Prior to cleaning, each sample was then subjected to hot uniaxial pressing experiments.

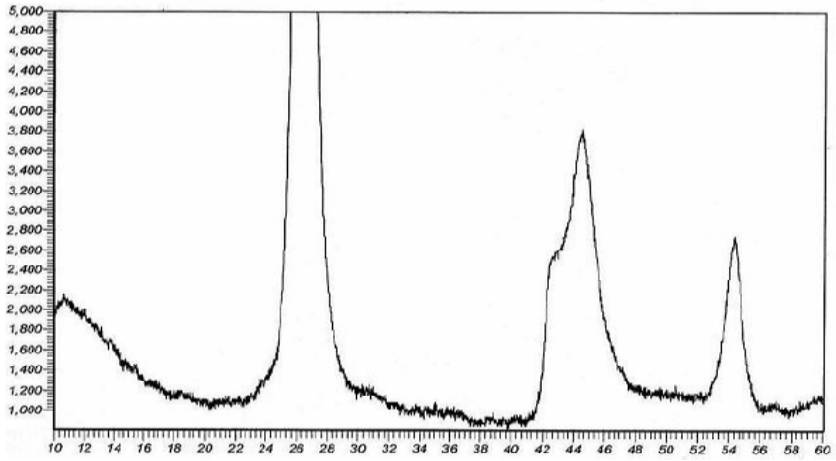

(a)

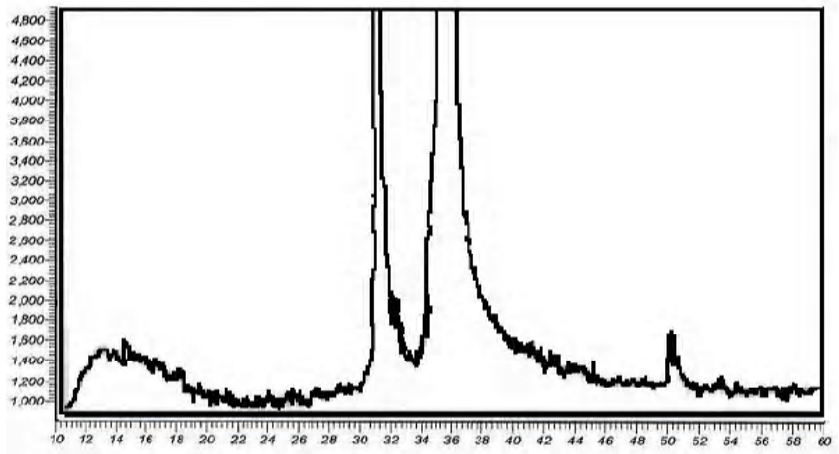

(b)

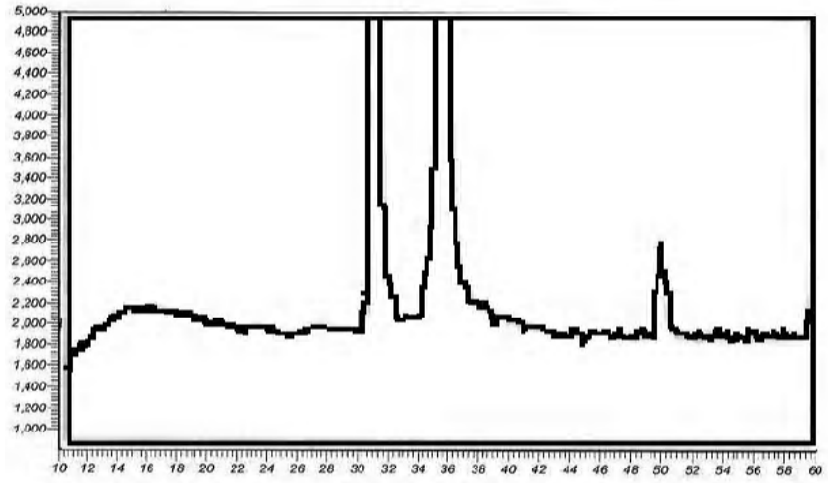

(c)

Fig. (1) Diffractograms from the surface of (a) graphite base material, (b) copper base material, and (c) copper base material after attempting the hot-pressing experiment

Copper is highly susceptible to oxidation and oxide skin is very tenacious even at high temperatures, even though in the presence of argon as inert atmosphere. To minimize the oxidation problem, a special vacuum system of ($0.15\text{-}0.18\text{x}10^{-2}$) N/m^2 was used. Most of copper oxidation problems associated with the heating experiments was eliminated.

In this study different heating temperature were used ranging from (700-850)°C, holding time was (30-120) min, and pressing pressure ($7.5\text{-}20\text{x}10^{6}$) N/m^2. Microstructural tests for

polished side of graphite were used using optical microscope, as shown in Fig. (2) and Fig. (3).

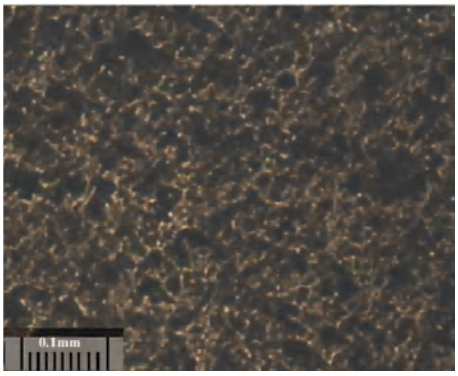

Fig. (2) Microstructure of graphite before attempting the hot uniaxial pressing

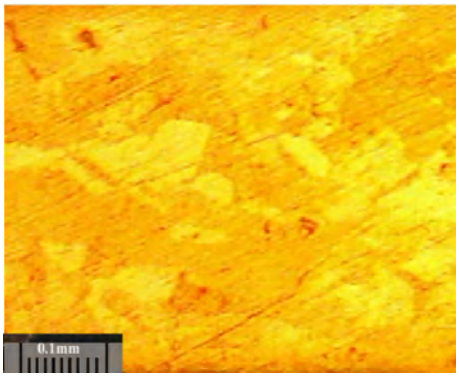

Fig. (3) Microstructure of copper before attempting the hot uniaxial pressing

3. Fractography and X-Ray Diffraction Analysis

After attempting the hot uniaxial pressing experiments for copper-graphite composites, fractography and XRD Analysis were used to examined the interfacial structure at the composites interface, the different features appeared could be classified as follows:

1- Diffusion of carbon at copper interface was observed and this was a function of changing heating temperatures (700-850)°C, were the diffusion is increased with increasing heating temperature. Figure (1c) shows Diffractograms from copper interface, indicating the effect of increasing heating temperature on diffusion of carbon through copper matrix. Figure (4) shows parallel lines of copper surface imprint at graphite interface and this was due to coarsening of graphite surface to increase the contact area. This procedure does not affect the newly formed contact region. Increase in heating time (30-120min), increases the recrystallization of copper (fine grains) but on the other hand does not affect the diffusion of carbon through interface markedly and this is clearly observed in Fig. (5).

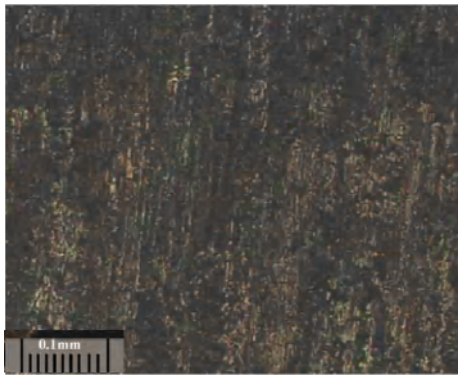

Fig. (4) Fractography at graphite interface, the effect of heating time after the hot uniaxial pressing

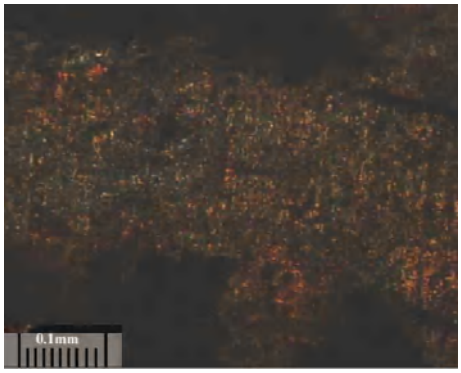

Fig. (5) Fractography at copper interface, the effect of heating time after the hot uniaxial pressing

2- Increasing the pressing load (7.5-20MPa) does not affect the diffusion of carbon through copper matrix markedly, and this was due to induced cracks during the pressing operation and this inhibit diffusion as well [14]. Figure (6) is a fractograph of copper, the dark area on the top of the micrograph represent the graphite adhered material, and the white area at the bottom of the micrograph represent copper contact interface, there is no diffusion of carbon in this region.

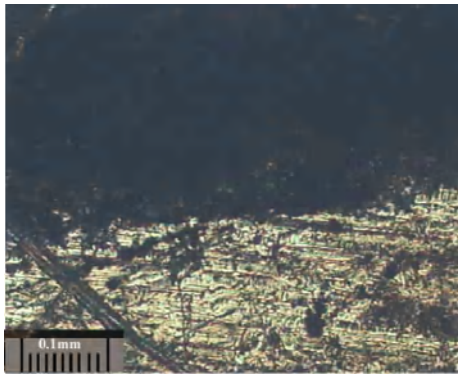

Fig. (6) Fractography of copper, the effect of pressing load inhibit diffusion significantly

3- The inert atmosphere had a significant effect on the reliability of the hot- pressing operation. The high oxidation of copper had a tailorable effect at high temperature and this

ISSN 1813-2065

induces an interfacial corrosion at interface, this inhibits the diffusion of carbon through copper matrix. As a result the oxide film became a barrier to form contact or bond, as shown in Fig. (7). Vacuum atmosphere ($0.15\text{-}0.18\text{x}10^{-2}$) N/m^2 is more reliable than argon atmosphere to achieve adhesion, and this agrees well with previous study of joining copper to ceramic [15].

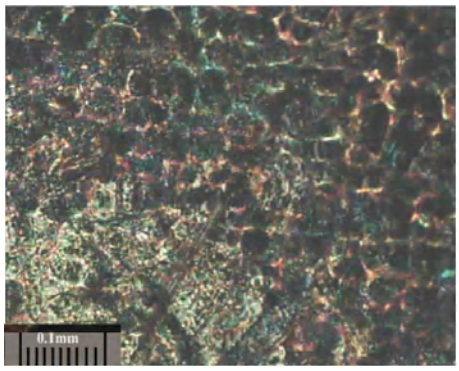

Fig. (7) Fractography of copper, the oxidation of copper surface due to argon atmosphere

4- The adhesion between copper ad graphite was achieved, and this was due to mechanical or interlocking theory. However, there is no intimate contact between the copper and graphite film [16], as shown in Fig. (8) and Fig. (9).

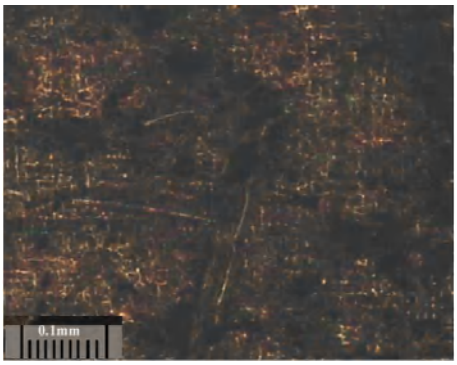

Fig. (8) Fractography of copper, the diffusion of carbon is observed at joint interface

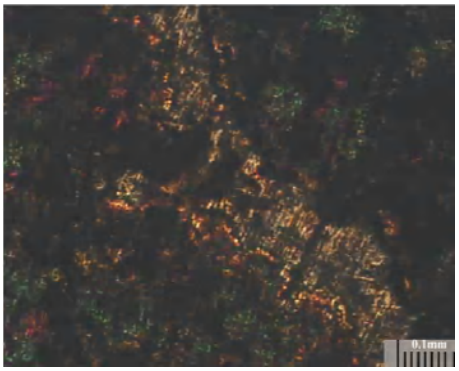

Fig. (9) Fractography of copper, were no intimate contact is formed

5- The increase in heating temperature enlarges the contact area during the hot uniaxial pressure experiments at interface and this is clearly observed in Fig. (10), (large dark area, is graphite bonded to copper interface), even though, the failure was observed during cooling to room temperature at graphite bulk material near joint interface for adhesive joint. On the other hand, failure occurs at copper- graphite interface as shown in Fig. (11), (grey regions represent graphite films bonded to copper and black spots represent graphite partitions) were weak boundary layered is formed, this is in reasonable agreement with the result reported [11,17].

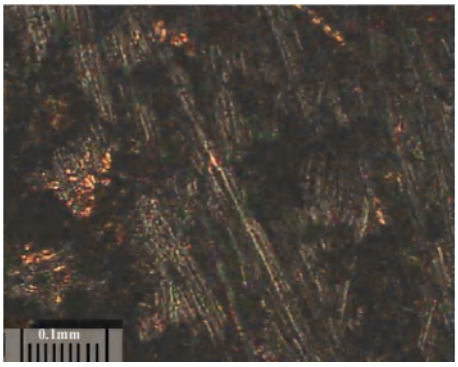

Fig. (10) Fractography of copper, weak boundary layered is formed

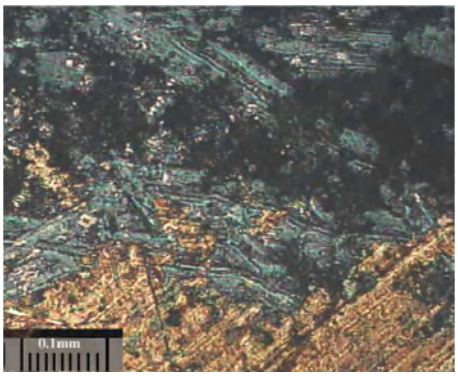

Fig. (11) Fractography of copper, failure was observed at graphite bulk material near interface

4. Conclusions

The experiments with the copper-graphite composite showed a dramatically different behavior. Hot uniaxial pressing parameters had a noticeable effect on diffusion of carbon and the resultant adhesion of graphite through copper matrix at the interfacial region. Obviously carbon does not wet copper, so the proposed mechanism for producing copper-carbon composite in solid state is, mechanical interlocking. The main effective parameter in improving composite reliability is, temperature. The diffusion of carbon at copper interfaces increased with increasing heating temperature and has it

maximum values at 850°C. Heating time has no considerable effect on diffusion through interfacial interface.

Increasing the pressing load during the hot uniaxial pressing operation induce cracks through graphite and inhibit diffusion of carbon through copper matrix. The effect of inert atmosphere appeared to be very effective at elevated temperature and implies that vacuum atmosphere ($0.15\text{-}0.18x10^{-2}$) N/m^2 is more reliable than argon atmosphere for overcoming the problem of copper corrosion at high temperature. The adhesion between copper ad graphite is achieved. However, there is no intimate contact between the copper and graphite film at interface. For all specimens the failure was observed through cooling to ambient temperature. This failure has two features. Firstly one at graphite bulk material near joint interface for adhesive joint, secondly at copper- graphite interface, where weak boundary layered is formed.

References

[1] J.G. Baetz, "Metal Matrix Composites: Their time has came", Aerospace America, November, (1998), 14-16.

[2] W.D. Callister Jr., **"Material Science and Engineering: an Introduction"**, John-Wiley & Sons, Inc., USA (2000) 186.

[3] K. Chawla and A. Meyers, **"Mechanical Behavior of Materials"**, Simon and Schuster, A Viacom Company (1998) 322-341.

[4] D.R. Tenny, G.F. Sykes and D.E. Bowles, "Composite Materials for Space Structures", Proc. 3rd Euro. Symp., Spacecraft Materials in Space Environment, European Space Agency (October 1985) 9-21.

[5] S. Rawal, *JOM*, 53(4) (2001) 14-17.

[6] H. Ohmura et al., *Welding J.*, 73(10) (1994) 2495-2565.

[7] H.I. Salah "Evaluation of Graphite/Graphite Brazing", M.Sc. Thesis, University of Technology, Department of Production and Metallurgy Engineering, Baghdad, Iraq (2005) 40-55.

[8] K. Landry, S. Kalogeropulou and N. Eustathopoulos, *Mater. Sci. and Eng.*, A254 (1998) 99-111.

[9] S.W. Ip et al., *Mater. Sci. and Eng.*, A244 (1998) 31-38.

[10] C. Beraud et al., *J. Mater. Sci.*, 24 (1989) 4545-4554.

[11] A.M. Ali, "The Investigation and characterization of Copper-Graphite Composites", M.Sc. Thesis, University of Technology, School of Applied Sciences, Baghdad, Iraq (2003) 33-44.

[12] Handbook of Applied Engineering Science, 2nd ed., Chemical Rubber Co., CRC Press, (2001) 23.

[13] Y.S. Touloukiav and R. Kirby, "Thermophysical Properties of Matter", the TBRC Data Series, Vol.12, Thermal Expansion, Metallic elements and Alloys, (1975) 1216-1243.

[14] N.F. Kazakov, **"Principal Bonding Variables and Recommended Procedures for Diffusion Bonding in Vacuum"**, MIR Publishers (Moscow, 1985) 49-69.

[15] S.A. Allamiy, "Diffusion Bonding of Alumina to Inconel600 using Cu Interlayer", Ph.D. Thesis, University of Technology, Department of Production and Metallurgy Engineering, Baghdad, Iraq (2007) 91-97.

[16] D.F. Porter and K.E. Easterling, **"Phase Transformation of Metals and Alloys"**, Chapman and Hall, Sweden (1990) 142-150.

[17] A.M. Brown and M.I. Ashby, *Acta Metallurgica*, 28 (1980) 1085-1101.

Reviewing codes: AP0208/2010/01/SPA, AP0208/2010/02/EGY

Scientists create artificial mini "Black Hole"

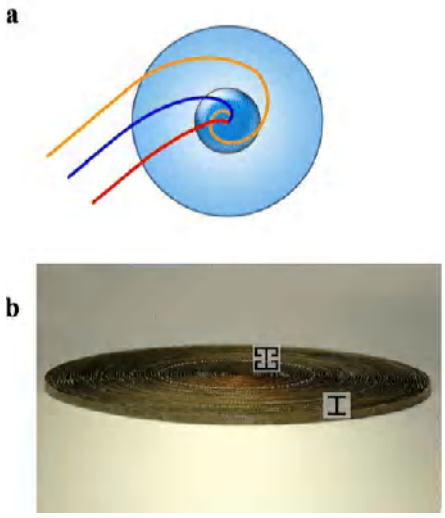

(a) A model of an electromagnetic omnidirectional absorber composed of a gradient-index metamaterial shell and a lossy dielectric core. (b) Photograph of the fabricated artificial omnidirectional absorbing device based on metamaterials, which is composed of 60 concentric layers, with ELC structures in the core layers and I-shaped structures in the shell layers.

Chinese researchers have successfully built an electromagnetic absorbing device for microwave frequencies. The device, made of a thin cylinder comprising 60 concentric rings of metamaterials, is capable of absorbing microwave radiation, and has been compared to an astrophysical black hole (which, in space, soaks up matter and light).

Abstract. ***In a recent theoretical work by Narimanov and Kildishev (2009 Appl. Phys. Lett. 95 041106) an optical omnidirectional light absorber based on metamaterials was proposed, in which theoretical analysis and numerical simulations showed that all optical waves hitting the absorber are trapped and absorbed. Here we report the first experimental demonstration of an omnidirectional electromagnetic absorber in the microwave frequency. The proposed device is composed of non-resonant and resonant metamaterial structures, which can trap and absorb electromagnetic waves coming from all directions spirally inwards without any reflections due to the local control of electromagnetic fields. It is shown that the absorption rate can reach 99 per cent in the microwave frequency. The all-directional full absorption property makes the device behave like an `electromagnetic black body', and the wave trapping and absorbing properties simulate, to some extent, an `electromagnetic black hole.' We expect that such a device could be used as a thermal emitting source and to harvest electromagnetic waves.***

The research published today, Thursday, 3 June, in *New Journal of Physics* (co-owned by the Institute of Physics and German Physical Society), shows how the researchers utilised the special properties of metamaterials, a class of ordered composites which can distort light and other waves.

Qiang Cheng and Tie Jun Cui of the State Key Laboratory of Millimeter Waves at Southeast University in Nanjing, China, designed and fabricated their absorbing device, officially called an "omnidirectional electromagnetic absorber", using 60 strips of circuit board arranged in concentric layers coated in copper. Each layer is imprinted with alternating patterns, which resonate or don't resonate in electromagnetic waves.

The designed device can trap and absorb electromagnetic waves coming from all directions by spiraling the radiation inwards and converting its energy into heat with an absorption rate of 99%. Hence it behaves like an "electromagnetic black body" or an "electromagnetic black hole".

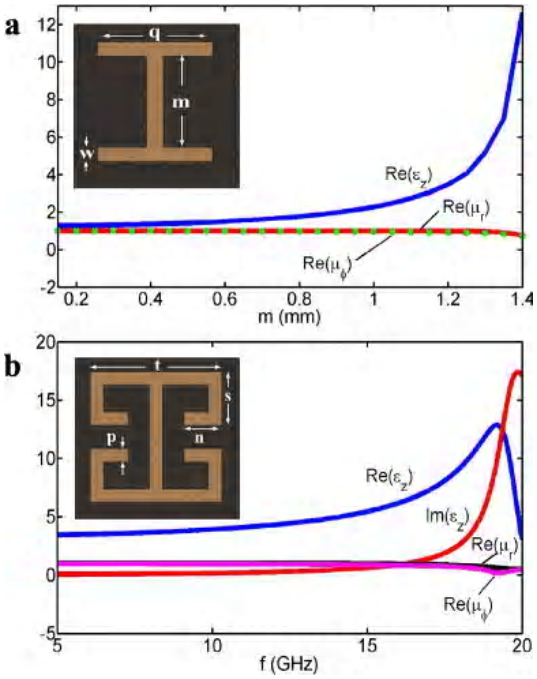

Effective medium parameters for unit cells of the artificial omnidirectional absorbing device. (a) The relation between the effective permittivity and permeability and the geometry dimension m for the I-shaped unit. The inset shows the sketch of the I-shaped unit, with w = 0.15 mm and q = 1.1 m. (b) The effective permittivity and permeability versus the frequency for the ELC resonator. The inset shows the sketch of the ELC unit, where t=1.6 mm, g=0.3 mm, p=0.15 mm, and s=0.65 mm.

At the moment, the device only works with microwaves, but the researchers are planning to develop a black hole for visible light next.

The current results could find some applications in microwaves. As the researchers write, "The good agreement between theoretical and experimental results has shown the excellent ability for metamaterials as the candidate to construct artificial omnidirectional absorbing devices.

"Since the lossy core can transfer electromagnetic energies into heat energies, we expect that the proposed device could find important applications in thermal emitting and electromagnetic-wave harvesting."

Determination of The Satellite Images Orientation Using DCT Coefficients

Hameed M. Abdul Jabar[1]
Mutasim I. Malik[2]

[1] *Department of Physics, College of Education Ibn Al-Haitham, University of Baghdad, Baghdad, Iraq*
[2] *Department of Physics, College of Science, University of Wasit, Kut, Iraq*

In this research a new method that determine the difference in orientation between two images (windows) using the DCT coefficients as descriptors is present, where the four operators that may change the orientation between the two images (windows) is studied by analyzing the new distribution of the DCT coefficients after applying each of them or their combinations. To determine the difference in orientation using the new distribution of the DCT coefficients, a new criterion is proposed which uses the sign changing in certain DCT coefficients as a pattern for that difference, and according to the results it success to determine the difference in the orientation between two images (windows) in very fast and accurate manner that invariant to the size and the details of the image (window).

Keywords: Image processing, Adjusting images orientation, DCT, Descriptors
Received: 10 February 2010, **Revised**: 19 March 2010, **Accepted**: 31 May 2010

1. Introduction

In many field of image processing and remote sensing adjusting the orientation between different images or their slide windows to be matched is common issue as pre or post processing step. Adjusting the orientation utilizes testing all possible different directions that may make the images orientation match, this process usually perform using pixel-based distance criteria in which the minimum of the sum squared distances between the images is intend [1].

Adjusting the orientation between different images are rise in many different fields, therefore many researches that deal with that issue are reported and all are aim to perform it with more accurate and efficient way that consume the computer less time and memory. In building 3-dimensional representation for big object, Besl and McKay [2] present iterative closest point (ICP) method to adjust the orientation of range images, the ICP searches corresponding points as the nearest neighbors between two range images. Relative rotation and translation matrices are computed so that the mean square error of the corresponding points is minimized. These steps are iterated until the error falls below the threshold value. Oishi [3] developed a faster model of the ICP method to reduce the computational time by reduce the algorithm to only three or more of the range image. In medical imaging, Bulan and Ozturk [4] present a comparison between a k-dimensional tree based alignment with the standard distance map based alignment algorithm, the k-dimensional based technique uses modified approximate nearest neighbor library, which primate to search in multidimensional space and adjust the orientation in 3D dataset of rodent brain. In remote sensing field Cheng [5] uses a binary image region based method to adjust the orientation between images by a two steps, first determine the overlap regions between the images and then the regions process to binary images, and then the binary images are filtered by mathematic morphologic method. In the appointed binary image region of the former image, feature template is searched and extracted. Through the XOR operation of the feature template and search region, some possible matching positions in the overlapped region of the latter image are obtained. In Image Processing, Dong and Guan [6] used the local binary pattern technique to adjust the images orientation, which is recognized as gray scale and rotation invariant, but this technique is variant for flipping and scaling or their combinations.

In the field of remote sensing, the standard four operations that may produce the difference in orientation between different images or there slide windows are flipping, rotation, scaling, translation, or combinations of these operations. The common way to adjust the orientation is to use the distance criteria to decide which orientation match the other image (window) better than the others orientation, therefore each image (window) should be tested using the four standard operations or there combinations and calculate the difference with the reference images (window).

2. DCT Coefficients as Descriptors

One of the properties that the DCT transform is possessing the energy compactness [7], which mean that the DCT transform has the ability to describe the image orientation in its coefficients (except the DC coefficient), therefore using the DCT transform as image (window) descriptor will provide a very fast way to detect the orientation of different images (windows) since there is no need for applying the four standard operations or there combinations and measure the distance between the images (windows).

In order to use the DCT transform as a descriptor there is a need to study the new distribution of the coefficients and their alternation to make pattern of changing for each standard operation or there combinations to use them to detect the orientation between the two images (windows).

3. Research Procedures

To maintain the generality and to make the results independent on the used images, random number generator used to generate the test slide windows for different sizes, which used to analyze the DCT coefficients. The coefficients of each generated slide window compared with the coefficients of the same generated slide window but after applying rotation, flipping, scaling, and\or translation operator separately and together (companied). The alteration in the DCT coefficients after applying the operators is detected using the DCT descriptor.

4. Results and Discussions

By comparing the DCT coefficients of the test slide windows before and after applying the operators, the alterations in the DCT coefficients illustrated in Fig. (1) is determined.

In Table (1), summary of the alteration in the DCT coefficients distribution and their signs is presented, in which for each operation(s) there is standard distribution for the new DCT coefficients. For some cases, when applying the operators together it will produced effect on the test slide windows similar to the effect of other operators and this is due to the symmetry effect of these operators.

Table (1) Summery of the changing in the DCT coefficients

Operation	Equal to	Sign Changing	Transpose
Flipping Around Rows (**r**)	**c180**	Yes	No
Flipping Around Columns (**c**)	**r180**	Yes	No
Rotation 90 Counterclockwise (**90**)	**90**	Yes	Yes
Rotation 180 Counterclockwise (**180**)	**180**	Yes	No
Rotation 270 Counterclockwise (**270**)	**270**	Yes	Yes
Flipping Around Rows And Rotation 90 Counterclockwise (**r90**)	**c270**	Yes	Yes
Flipping Around Rows And Rotation 180 Counterclockwise (**r180**)	**C**	Yes	No
Flipping Around Rows And Rotation 270 Counterclockwise (**r270**)	**c9o**	No	Yes
Flipping Around Columns And Rotation 90 Counterclockwise (**c90**)	**r270**	No	Yes
Flipping Around Columns And Rotation 180 Counterclockwise (**c180**)	**r**	Yes	No
Flipping Around Columns And Rotation 270 Counterclockwise (**c270**)	**r90**	Yes	Yes

By examining Fig. (1), it is clear that the DCT coefficient altered with the four operators in two manners either by altering the sign of some coefficients in certain pattern for each operation or altering the coefficients by two steps first by altering the sign and then by transpose the coefficients.

By studying the alteration in the DCT coefficients it is easy to notice that the new distribution of the DCT coefficients after applying the four operators or their combinations is invariant for the size and contain of the original data (image details) as shown in Fig. (1). That's make the determining of which operator(s) that may produce the new distribution of the DCT coefficients is easy by comparing them with the DCT coefficients of the original data. In this research a new criteria is suggested to determine the difference in orientation between two datasets by taking certain coefficients and determine if the signs of them are changed and according to the sign changing pattern the difference in the orientation between the datasets is determine (i.e. which of the four operators or their combinations caused the difference).

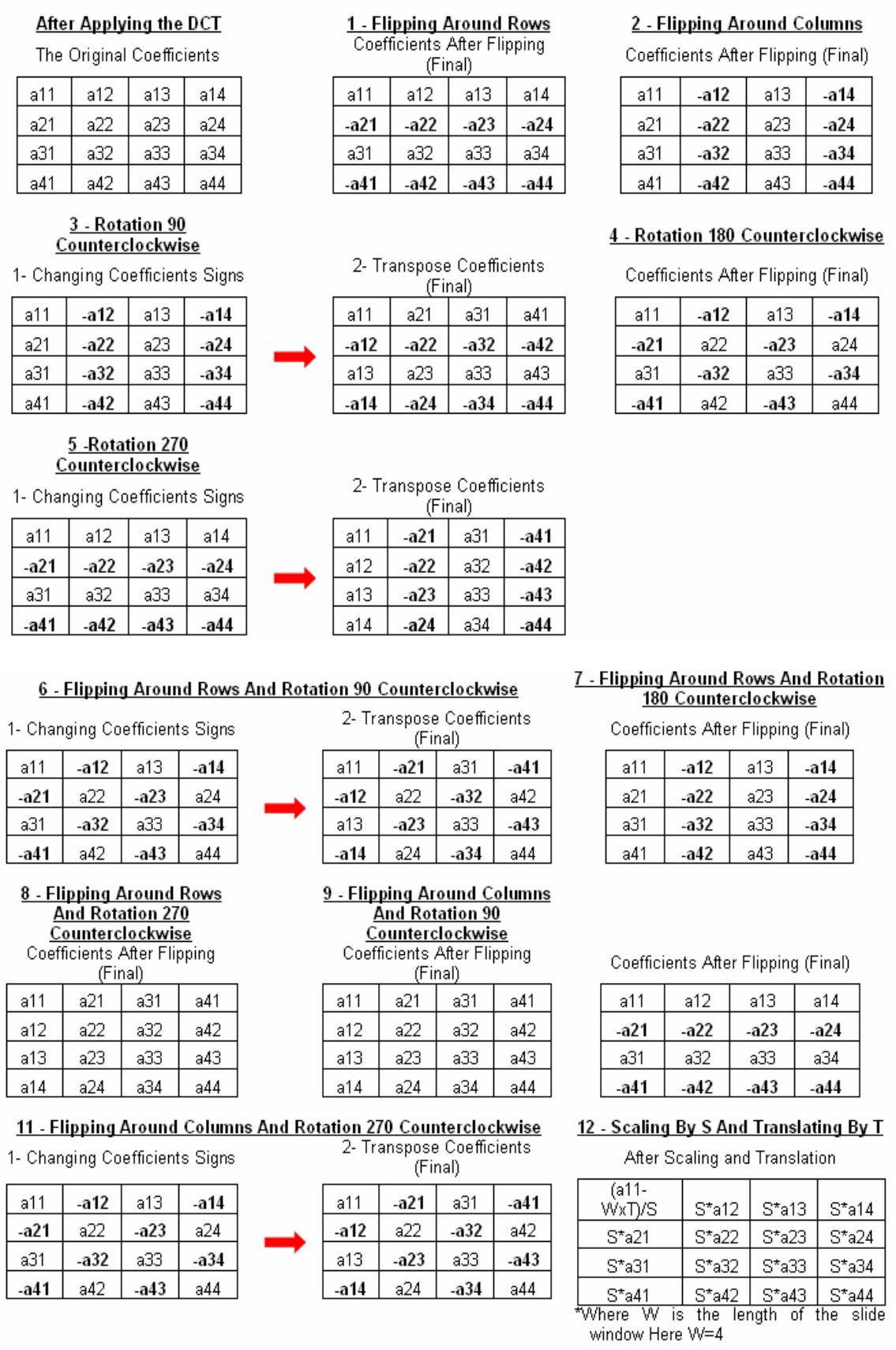

Fig. (1) the changing in the DCT coefficients with slide window of size 4x4 pixel

ISSN 1813-2065

In this new criteria, the coefficients election is done after a careful study for the new distribution of the DCT coefficients comparing with the original DCT coefficients, which let us elect eight coefficients (which can be reduce to four) that their sign change can be used as a pattern to determine the difference in orientation between any two dataset as shown in Table (2). The changing in sign for any coefficient can be tested by simply multiplying this coefficient with the same coefficient in the original DCT coefficients (has same location) and see if the multiplying result is negative which mean that the sign is changed and vice versa.

Table (2) the changing sign pattern that determine the difference in orientation, where the O means that the two coefficients have the same sign and X mean that the two coefficients have different signs (capital letters mean after applying the operator(s) and small for the original DCT coefficient)

	a21*A21	a32*A32	a12*A21	a23*A23	a21*A12	a41*A14	a24*A24	a43*A34
r	X	O		X			X	
c		X		O			X	
90			X		O	O		O
180	X		X	X			O	
270			O		X	X		X
r90			X		X	X		X
r180	O	X		O			X	
r270			O		O	O		O

5. Conclusions

According to the obtained results, the following conclusions are driven. For each operation of the four operations (or their combinations), the DCT coefficients will be always changed in a certain pattern. The new pattern of the DCT coefficients after applying one or combination of the four operations is invariant with the window size and details. In some cases of combining two of the four operators together, it will produce the same effect when combine other two operators as shown in Table (1), therefore they will produce the same distribution for the DCT coefficients. The suggested criterion success to determine the difference in orientation in very fast and accurate way and it is invariant for dataset size or contained.

References

[1] R. Szeliski, "Image Alignment and Stitching: A Tutorial", Technical Report, MSR-TR-2004-92, Microsoft Corporation (2006) p.16.

[2] P.J. Besl and N.D. Mckay, *IEEE Trans. on PAMI*, 14 (1992) 239-256.

[3] T. Oishi et al., *Proc. 5th Int. Conf. on IEEE 3-D Digital Imaging and Modeling, 3DIM*, (2005) 476-483.

[4] G. Bulan and C. Ozturk, *IEEE Proc. of 23rd Annual Int. Conf. of the Engineering in Medicine and Biology Society, EMBS*, Vol.3 (2001) 2606-2608.

[5] Y. Cheng, D. Xue and Y. Li, *IEEE Int. Conf. on Mechatronics and Automation, ICMA 2007*, 2009-2013.

[6] N. Dong and L. Guan, *IEEE Int. Workshop on Multimedia Signal Processing, MMSP'09* (2009) 1-5.

[7] Y. Wu and S. Tai, *IEEE Trans. on Consumer Electronics*, CE-43(2) 134-140, 1997.

Reviewing codes: AP0185/2010/01/CHN, AP0185/2010/02/EGY

THE IRAQI JOURNAL OF APPLIED PHYSICS
EDITORIAL BOARD

COPYRIGHT RELEASE
Iraqi Journal of Applied Physics (IJAP)

We, the undersigned, the author/authors of the article titled
……
……
……
……
……
……
that is presented to the Iraqi Journal of Applied Physics (IJAP) for publication, declare that we have neither taken part or full text from any published work by others, nor presented or published it elsewhere in any other journal. We also declare transferring copyrights and conduct of this article to the Iraqi Journal of Applied Physics (IJAP) after accepting it for publication.

The authors will keep the following rights:
1. Possession of the article such as patent rights.
2. Free of charge use of the article or part of it in any future work by the authors such as books and lecture notes without referring to the IJAP.
3. Republishing the article for any personal purposes of the authors after taking journal permission.

To be signed by all authors:

Signature:……..date: ……

Printed name: ……

Signature:……..date: ……

Printed name: ……

Signature:……..date: ……

Printed name: ……

Correspondence address:……...
……..
Address:……
……
……
Telephone:……..email: ……..

Note: Please complete and sign this form and mail it to the below address with your manuscript

The Iraqi Journal of Applied Physics
P. O. Box 55259, Baghdad 12001, IRAQ
Website: www.ijap.org
Email: editor@ijap.org
Phone: +964 7901274190

IRAQI JOURNAL OF APPLIED PHYSICS

CONTENTS

Instructions to Authors		**2**
Numerical Model to Estimate the Potential Changes within Laser-Solid Surface Interaction Zone	**N.I. Naji A.-M.I. Ahmed**	**3-11**
Physicists find a big particle accelerator in the sky (*essay*)		**12**
Curvelet-Based Optical Flow Estimation Algorithm Based on Central Derivatives	**A.A. Sabri**	**13-18**
Design and Analysis of Special Small Size Cross Dipole Antenna	**F.J. Jibrael**	**19-23**
SPIE "Society of Photonics Instrumentation Engineers", Scientific Calendar		**24**
Microstructural Study of Copper-Carbon Composite Interface	**A.A.-R. Abdullah**	**25-29**
Scientists create artificial mini "Black Hole" (*essay*)		**30**
Determination of The Satellite Images Orientation Using DCT Coefficients	**H.M. Abdul Jabar M.I. Malik**	**31-34**
Contents		**36**

